

UNCLASSIFIED

Defense Technical Information Center
Compilation Part Notice

ADP012368

TITLE: Direct Numerical Simulations of LOX/H₂ Temporal Mixing Layers Under Supercritical Conditions

DISTRIBUTION: Approved for public release, distribution unlimited

This paper is part of the following report:

TITLE: 2nd International Workshop on Rocket Combustion Modeling: Atomization, Combustion and Heat Transfer held in Lampoldshausen, Germany on 25-27 Mar 2001

To order the complete compilation report, use: ADA402618

The component part is provided here to allow users access to individually authored sections of proceedings, annals, symposia, etc. However, the component should be considered within the context of the overall compilation report and not as a stand-alone technical report.

The following component part numbers comprise the compilation report:
ADP012355 thru ADP012373

UNCLASSIFIED

DIRECT NUMERICAL SIMULATIONS OF LOX/ H_2 TEMPORAL MIXING LAYERS UNDER SUPERCRITICAL CONDITIONS

Nora Okong'o, Kenneth Harstad and Josette Bellan*

Jet Propulsion Laboratory
California Institute of Technology
4800 Oak Grove Drive
Pasadena, CA 91109-8099

Abstract

Direct Numerical Simulations (DNS) of a supercritical LOX/ H_2 temporal three-dimensional mixing layer are conducted for the purpose of exploring the features of high pressure mixing behavior. The conservation equations are formulated according to fluctuation-dissipation (FD) theory which is not only totally consistent with non-equilibrium thermodynamics, but also relates fluxes and forces from first principles. According to FD theory, complementing the low-pressure typical transport properties (viscosity, diffusivity and thermal conductivity), the thermal diffusion factor is an additional transport property which may play an increasingly important role with increasing pressure. The Peng-Robinson equation of state with a correction for obtaining accurate molar volumes, in conjunction with appropriate mixing rules, is coupled to the dynamic conservation equations to obtain a closed system. The boundary conditions are periodic in the streamwise and spanwise directions, and of non-reflecting outflow type in the cross-stream direction. Following the DNS protocol, the studied temperature/pressure regime is one where both Kolmogorov and Batchelor scales can be resolved for pseudo-species (i.e. species with transport properties modified to allow the attainment of large enough Reynolds numbers). Correlations for the Schmidt and Prandtl numbers as functions of the thermodynamic variables, based on exact fluid properties, are used to ensure that correct relative transport processes are employed. To obtain rollup and pairing, the layer is perturbed similarly to heptane/nitrogen mixing layers that achieved transition in previous investigations. Due to the strong density stratification, the layer is considerably more difficult to entrain

*Corresponding author: josette.bellan@jpl.nasa.gov

than equivalent initial Reynolds number gaseous, droplet-laden or supercritical heptane/nitrogen layers. Simulations conducted with initial Reynolds numbers of 600 and 750, an initial convective Mach number of 0.4, an initial pressure of 100 atm. and freestream temperatures of 400 K in the lower LOX and 600 K in the upper H_2 stream, eventually exhibit distorted regions of high density gradient magnitude similar to the experimentally observed wisps of fluid at the boundary of supercritical jets. The temperature stratification was chosen such that the computation can be spatially resolved at these Reynolds numbers, accounting for memory constraints. In these simulations the layer does not exhibit transition to turbulence, although they are conducted with an initial Reynolds number and perturbation for which transition was obtained for a heptane/nitrogen mixing layer having a smaller initial density stratification. The cause of this occurrence is analyzed using global growth characteristics, vorticity and vorticity-magnitude budgets, instantaneous visualizations of the dynamic and thermodynamic variables and an inspection of the origins and spatial location of dissipation. The lack of transition is traced to two combined effects. First, the relatively large spanwise perturbation is responsible for the early creation of small turbulent scales which destroy the coherence of the vortices formed through pairing, resulting in a weakened ultimate vortex. Second, regions of high density gradient magnitude are formed due both to the distortion of the initial density stratification boundary and to the mixing of the two species: in these regions, the weakened vortex cannot create the small turbulent scales that are crucial to mixing transition.

1 Introduction

Liquid rocket propulsion relying on hydrogen/liquid-oxygen (LOX) combustion is not a mature technology in that improvements in design are still necessary to mitigate efficiency and stability problems. To solve these problems in a systematic manner, it is required to understand the fundamental processes occurring in liquid rocket chambers. A simplified description of the sequence of events in one of these combustion chambers is as follows: LOX enters the chamber through one of the many injection ports, and irrespective of the exact injection configuration, LOX disintegrates, mixes with H_2 in a highly turbulent manner while being ignited, with ensuing combustion producing water and other incomplete combustion products. From this description, it is immediately clear that LOX disintegration plays a crucial role in determining the size of the LOX parcels entering in contact with H_2 , and further the efficiency of the combustion process.

LOX disintegration is a process essentially different from the much studied spray atomization that involves the breakup of a liquid into a multitude of drops. Liquid breakup relies on physical mechanisms involving the surface tension, and therefore it is an appropriate concept only when a surface tension does indeed exist. In contrast, in liquid rocket chambers the mean pressure is about 20 MPa, with peaks as high

as 30 MPa, and therefore both LOX and H_2 are in a supercritical state (see Table 1). By definition [1], a substance is in a supercritical state when it is at a pressure, p , or temperature, T , exceeding its critical value (indicated here by a subscript c). What truly characterizes the supercritical state is the impossibility of a two phase region. Indeed, when the reduced pressure, $p_r \equiv p/p_c > 1$ or the reduced temperature $T_r \equiv T/T_c > 1$, in the (p, T) plane there is no longer the possibility of a two phase (i.e. gas/liquid) region, and instead there is only a single-phase region [2]. The general term for the substance is fluid, i.e. neither a gas nor a liquid. Noteworthy, since the critical locus of O_2/H_2 mixtures may include smaller or higher values of (p_c, T_c) than those of the pure species, it is possible that locally in space and time the mixture could be at subcritical conditions, but such a situation cannot be assumed to hold for any amount of time owing to the continuous change in the mixture composition. Moreover, Harstad and Bellan [3] concluded from their study of the evolution of an initial LOX fluid drop immersed in H_2 at pressures from 6 to 40 MPa, that nowhere in the fluid drop or in the fluid mixture surrounding it, are critical or subcritical conditions reached. The indications from this study as well as recent LOX/ H_2 experimental evidence from Mayer et al. [4], [5] is that LOX disintegration assumes characteristics different from atomization, and that these characteristics reflect features associated with supercritical conditions. In contrast to the process of atomization, past the critical point of the fluid, disintegration assumes the aspect of what Chehrودي et al. [6] call ‘fingers’, or ‘comb-like structures’ at transcritical conditions, having an increasingly gaseous appearance with increasing pressure; their experiments were conducted with N_2/N_2 , $N_2/(CO+N_2)$, He/N_2 and O_2/N_2 . Related to the present study, Raman scattering measurements of the radial density in free N_2 jets at 4 MPa by Oschwald and Schik [7] show sharp profiles independent of the injection temperature, indicating the occurrence of sharp density gradients. These regions of sharp density gradients are indeed one of the distinctive optical features in environments at supercritical conditions. Not only have they been experimentally observed, but they have also been identified in simulations of heptane/nitrogen three-dimensional mixing layers (see Miller et al. [8], and Okong’o and Bellan [9]). Analysis of an enlarged database of Miller et al. [8] by Okong’o and Bellan [10] revealed that these regions of large density gradient magnitude play a crucial role in delaying transition to turbulence by acting similar to material surfaces in that they damp emerging turbulent eddies.

Because the behavior of a binary species system depends on the identity of the species, it is uncertain if our previous findings for heptane/nitrogen are immediately applicable to the LOX/ H_2 system which is here of interest. For example, Harstad and Bellan [11] found that under supercritical conditions, compared to the heptane/nitrogen combination, the LOX/ H_2 system displays an increased solubility, and also much larger effective Lewis numbers, Le_{eff} . The increased solubility results from the thermodynamic mixing rules [1], whereas the enhanced effective Lewis numbers were attributed to the considerably larger difference of the specific (i.e. mass based)

enthalpies of the components in the LOX/ H_2 system compared to the equivalent difference for heptane/nitrogen.

The present paper is devoted to the study of LOX/ H_2 three-dimensional (3D) mixing layers through Direct Numerical Simulations (DNS) as a means of obtaining information about its specific behavior. Since in DNS all scales of the flow are resolved, these simulations appear ideal for developing information to be used in modeling LOX disintegration, as well as turbulent LOX/ H_2 mixing. In Section 2 below we briefly recall the conservation equations derived elsewhere [8], [9]. Section 3 is devoted to describing the particular aspects of the equation of state implemented in the model such as to obtain increased accuracy with respect to the typical Peng-Robinson formalism. Further, in Section 4 we address the choice of the transport coefficients. The configuration and boundary conditions are addressed in Section 5, whereas in Section 6 we discuss the numerics. Section 7 focuses on the initial conditions and presents results from a linear, inviscid stability analysis which is used to understand specific aspects of the LOX/ H_2 mixing layer that are necessary for choosing initial conditions for the 3D simulations. In Section 8, we present two 3D simulations at different initial Reynolds numbers, Re_0 . The global characteristics of the layers show that despite the relatively large momentum thickness based Reynolds number, Re_m , neither of these two layers reached transition. To understand the origin of lack of transition attainment, we concentrate on detailed studies of the layer with the larger Re_0 and present the results of this analysis. A summary and conclusions appear in Section 9.

2 Conservation equations

The conservation equations are briefly recalled, and the reader is referred for details to Miller et al. [8], Okong'o and Bellan [9] and Okong'o et al.[12]. For the binary mixture under consideration, the conservation equations are

$$\frac{\partial \rho}{\partial t} + \frac{\partial (\rho u_j)}{\partial x_j} = 0, \quad (1)$$

$$\frac{\partial (\rho u_i)}{\partial t} + \frac{\partial (\rho u_i u_j + p \delta_{ij})}{\partial x_j} = \frac{\partial \tau_{ij}}{\partial x_j}, \quad (2)$$

$$\frac{\partial (\rho Y_O)}{\partial t} + \frac{\partial (\rho Y_O u_j)}{\partial x_j} = -\frac{\partial j_{Oj}}{\partial x_j}, \quad (3)$$

$$\frac{\partial (\rho e_t)}{\partial t} + \frac{\partial [(\rho e_t + p) u_j]}{\partial x_j} = -\frac{\partial q_{IKj}}{\partial x_j} + \frac{\partial \tau_{ij} u_i}{\partial x_j}, \quad (4)$$

where x is a Cartesian coordinate, t is time, ρ is the density, u_i is the velocity, $e_t = e + u_i u_i / 2$ is the total energy (i.e. internal energy, e , plus kinetic energy), p is the thermodynamic pressure (the temperature is T) and Y_O is the mass fraction of O_2 (the mass fraction of H_2 is $Y_H = 1 - Y_O$). Furthermore, \mathbf{q}_{IK} is the Irwing - Kirkwood (subscript IK) form of the heat flux vector (see Sarman and Evans [13]), \mathbf{j}_O is the heptane mass flux vector and τ_{ij} is the Newtonian viscous stress tensor

$$\tau_{ij} = \mu \left[\frac{\partial u_i}{\partial x_j} + \frac{\partial u_j}{\partial x_i} - \frac{2}{3} \frac{\partial u_k}{\partial x_k} \delta_{ij} \right], \quad (5)$$

where δ_{ij} is the Kronecker delta function, and μ is the mixture viscosity which is in general a function of the thermodynamic state variables. The mass flux and heat flux are given by

$$j_{Oj} = - \left[j'_{Oj} + (\alpha_{IK} - \alpha_h) Y_O Y_H \frac{\rho D}{T} \frac{\partial T}{\partial x_j} \right], \quad (6)$$

$$q_{IKj} = -\lambda'_{IK} \frac{\partial T}{\partial x_j} - \alpha_{IK} R_u T \frac{m}{m_O m_H} j'_{Oj}, \quad (7)$$

$$j'_{Oj} = \rho D \left[\alpha_D \frac{\partial Y_O}{\partial x_j} + \frac{Y_O Y_H}{R_u T} \frac{m_O m_H}{m} \left(\frac{v_{,O}}{m_O} - \frac{v_{,H}}{m_H} \right) \frac{\partial p}{\partial x_j} \right], \quad (8)$$

with

$$\alpha_h = \frac{1}{R_u T} \frac{m_O m_H}{m} \left(\frac{h_{,O}}{m_O} - \frac{h_{,H}}{m_H} \right). \quad (9)$$

The notation in eqs. 6 - 9 is as follows: D is the binary diffusion coefficient; α_D is the mass diffusion factor which is a thermodynamic quantity; m_α is the molar mass of species α ; $m = m_O X_O + m_H X_H$ is the mixture molar mass where the molar fraction $X_\alpha = m Y_\alpha / m_\alpha$; $v_{,\alpha} = (\partial v / \partial X_\alpha)_{T,p,X_\beta(\beta \neq \alpha)}$ is the partial molar volume and $h_{,\alpha} = (\partial h / \partial X_\alpha)_{T,p,X_\beta(\beta \neq \alpha)}$ is the partial molar enthalpy; $v = X_H v_{,H} + X_O v_{,O}$, is the molar volume related to the density by $v = m / \rho$, $h = X_H h_{,H} + X_O h_{,O}$ is the molar enthalpy; R_u is the universal gas constant and λ'_{IK} is a thermal conductivity defined from the transport matrix

$$\lambda'_{IK} = \lambda + X_H X_O \alpha_{IK} \alpha_{BK} R_u \rho D / m, \quad (10)$$

where $\lim_{p \rightarrow 0} \lambda = \lambda_{KT}$ as discussed in [14], where the subscript KT refers to Kinetic Theory. The new transport coefficients associated with the Soret (in the molar fluxes) and the Dufour (in the heat flux) terms of the transport matrix are α_{BK} and α_{IK} , which are the thermal diffusion factors corresponding to the IK and the Bearman-Kirkwood (subscript BK) forms of the heat flux (see Sarman and Evans [13]). These

transport coefficients are characteristic of each particular species pairs and they obey the relationship

$$\alpha_{BK} = \alpha_{IK} - \alpha_h, \quad (11)$$

as shown by Harstad and Bellan [14]. Additionally, $\lim_{p \rightarrow 0} \alpha_{IK} \neq \alpha_{KT}$ and $\lim_{p \rightarrow 0} \alpha_{BK} = \alpha_{KT}$.

To solve the system of equations above, it must be closed by specifying the equation of state (EOS) and the transport properties.

3 Equation of state

The pressure can be calculated from the well-known Peng-Robinson (PR) EOS given the PR molar volume, v_{PR} , as

$$p = \frac{R_u T}{(v_{PR} - b_m)} - \frac{a_m}{(v_{PR}^2 + 2b_m v_{PR} - b_m^2)}, \quad (12)$$

where a_m, b_m are functions of T and X_α (see Appendix A). Due to the inaccuracy of the PR EOS at high pressures (see [1]), v_{PR} may differ significantly from the actual molar volume v . Therefore for improved accuracy, we use a modified PR EOS in which both v_{PR} and the volume shift

$$v_S = v - v_{PR} \quad (13)$$

are calculated from the PR EOS given p, T and X_α .

All the thermodynamic properties such as the molar enthalpy, $h = G - T(\partial G / \partial T)_{p,X}$, the constant-pressure molar heat-capacity, $C_p = (\partial h / \partial T)_{p,X}$, and the speed of sound, $a_s = \sqrt{1 / \rho \kappa_s}$, are calculated in a consistent manner from the same EOS using the Gibbs energy, G :

$$G(T, p, X_\alpha) = \int_v^{v_u} p(v', T, X_\alpha) dv' + pv - R_u T + \sum_\alpha X_\alpha [G_\alpha^0 + R_u T \ln(X_\alpha)], \quad (14)$$

where the superscript 0 represents the 'low pressure' reference condition for the integration as generally used in the departure function formalism described by Prausnitz et al. [1]. The integral is ill defined for a zero pressure reference condition; hereinafter we choose $p^0 = 1 \text{ bar}$ such that $v_u = R_u T / p^0$. The volume shift v_S is calculated from G_α^0 (see Harstad et al. [15]) as

$$v_S = \sum_\alpha X_\alpha \frac{\partial G_\alpha^0}{\partial p}. \quad (15)$$

The isentropic compressibility, κ_s is calculated from

$$\kappa_s = \kappa_T - v T \alpha_v^2 / C_p, \quad (16)$$

where the expansivity (α_v) and the isothermal compressibility (κ_T) are given by

$$\alpha_v = -\frac{(\partial p/\partial T)_{v,X}}{v(\partial p/\partial v)_{T,X}}, \quad \kappa_T = \frac{-1}{v(\partial p/\partial v)_{T,X}}. \quad (17)$$

The mass diffusion factor, α_D , is calculated from the fugacity coefficients, φ_α (which are related to the Gibbs energy), through

$$\alpha_D = 1 + X_\alpha \frac{\partial \ln(\varphi_\alpha)}{\partial X_\alpha} \quad (18)$$

and portrays departures from mixture ideality (i.e. $\alpha_D = 1$). Noteworthy, α_D is independent of the species chosen in the calculation of eq. 18.

These equations specify the entire thermodynamics of the binary mixture.

4 Transport coefficients

DNS are calculations where both the Kolmogorov and Batchelor scales must be resolved. To ensure that this requirement is satisfied, we produced contour plots (not shown) of the viscosity, and of Sc and the Prandtl number, Pr , based on accurate species transport properties calculated as in Harstad and Bellan [16]. Based on these contour plots in the range 200K to 800K, the transport properties were correlated as

$$\mu = \mu_R \left(\frac{T}{(T_1 + T_2)/2} \right)^{0.75}; \quad T \text{ in Kelvins}, \quad (19)$$

$$Sc \equiv \frac{\mu}{\rho \alpha_D D} = (1.334 - 0.668Y_O - 0.186Y_O^2 - 0.268Y_O^6) \left[1 + \left(\frac{88.6}{T} \right)^{1.5} \right], \quad (20)$$

$$Pr \equiv \frac{\mu C_p / m}{\lambda} = \frac{1.335}{T^{0.1}}, \quad (21)$$

where μ_R is a reference viscosity and the reference temperatures T_1 (upper H_2 stream) and T_2 (lower O_2 stream) correspond to the free stream temperatures for mixing layer simulations.

The value of the reference viscosity is determined by the specified value of Re_0 (see below), chosen so as to enable the resolution of all relevant length scales.

The thermal diffusion factor is selected as in Harstad and Bellan [16] with $\alpha_{BK} = 0.2$, and α_{IK} is calculated from eq. 11.

5 Configuration and boundary conditions

The temporally developing mixing layer configuration is depicted in Fig. 1, which shows the definition of the streamwise (x_1), cross-stream (x_2) and spanwise (x_3) coordinates. The layer is not symmetric in extent in the x_2 direction, having found in our simulations that the layer growth is considerably larger in the hydrogen side. The freestream density (ρ_1 or ρ_2) is calculated for each pure species at its freestream temperature (T_1 or T_2) and at the initial uniform pressure (p_0). The vorticity thickness is defined as $\delta_\omega(t) = \Delta U_0 / (\partial \langle u_1 \rangle / \partial x_2)_{max}$ where $\langle u_1 \rangle$ is the $x_1 - x_3$ planar average velocity in the streamwise direction, and $\Delta U_0 = U_1 - U_2$ is the velocity difference across the layer. Miller et al. [8] explain the choice of the velocities of the two streams in a simulation initiated with four streamwise vortices pairing twice to produce an ultimate vortex. The choice of U_1 and U_2 for a real fluid

$$U_1 = 2M_{c,0}a_{s1} \left[1 + \left(\frac{a_{s1}}{a_{s2}} \right) \sqrt{\frac{\rho_1 Z_1}{\rho_2 Z_2}} \right]^{-1}, \quad U_2 = -\sqrt{\frac{\rho_1 Z_1}{\rho_2 Z_2}} U_1, \quad (22)$$

was made with the intent of keeping the ultimate vortex stationary in the computational domain, although the success of this strategy was only partial. Here $M_{c,0}$ is the convective Mach number and $Z = p/(\rho T R_u/m)$ is the compression factor indicating departures from the perfect gas behavior (i.e. $Z = 1$). The specification of $M_{c,0}$ therefore determines ΔU_0 . Given the initial streamwise velocity profile u_1 based on U_1 and U_2 , $(\partial \langle u_1 \rangle / \partial x_2)_{max}$ and hence $\delta_{\omega,0} \equiv \delta_\omega(0)$ are calculated.

The specified value of the initial flow Reynolds number,

$$\text{Re}_0 = \frac{0.5(\rho_1 + \rho_2)\Delta U_0 \delta_{\omega,0}}{\mu_R} \quad (23)$$

is used to calculate μ_R .

The boundary conditions are periodic in the streamwise and spanwise directions, and of outflow type for real gas as derived by Okong'o et al. [12]. The outflow type conditions are essential to maintain stability since the initial perturbation causes large pressure waves which must be allowed out of the domain with minimal reflection.

6 Numerics

6.1 General method

The conservation equations are numerically solved using a fourth-order explicit Runge-Kutta time integration and a sixth-order compact scheme for spatial derivatives ([17]). Time stability is achieved by filtering the conservative variables every five time steps in the interior, in each spatial direction alternately, using an eighth-order filter. Since high-order boundary filters are unstable, no filtering is applied at the non-periodic

(x_2) boundaries. The computations were parallelized using three-dimensional domain decomposition and message passing. The tridiagonal solver for the compact derivative scheme was efficiently parallelized using the method of [18]. The simulations were performed on an SGI Origin 2000 supercomputer, using 64 processors.

In our solution protocol, once the pressure, temperature, and mole fractions are calculated, the density and energy are calculated from the EOS. To calculate the pressure and temperature from the known energy and mole fractions, we iterate at each time step, as described below.

6.2 Iterative solution for the pressure and temperature

Using the modified Peng-Robinson equation of state [15], once (p, T, X_α) are specified, one can calculate (ρ, e, Y_α) . However, in the DNS the dependent variables are (ρ, e, Y_α) from which v and X_α are calculated as

$$m = \frac{1}{\sum_\alpha \frac{Y_\alpha}{m_\alpha}}, \quad X_\alpha = \frac{m Y_\alpha}{m_\alpha}, \quad v = \frac{m}{\rho}. \quad (24)$$

This means that an iteration is necessary to obtain the values of (p, T) corresponding to the DNS (ρ, e) . The procedure for this iteration is to update (p, T) at iteration level n , (p^n, T^n) , using:

$$T^n = T^{n-1} + dT, \quad p^n = p^{n-1} + dp, \quad (25)$$

$$dT = \left(\frac{\partial T}{\partial v} \right)_{e, X_\alpha}^{n-1} dv + \left(\frac{\partial T}{\partial e} \right)_{v, X_\alpha}^{n-1} de + \sum_\alpha \left(\frac{\partial T}{\partial X_\alpha} \right)_{v, e, X_\beta}^{n-1} dX_\alpha, \quad (26)$$

$$dp = \left(\frac{\partial p}{\partial v} \right)_{v, X_\alpha}^{n-1} dv + \left(\frac{\partial p}{\partial e} \right)_{v, X_\alpha}^{n-1} de + \sum_\alpha \left(\frac{\partial p}{\partial X_\alpha} \right)_{v, e, Y_\beta}^{n-1} dX_\alpha. \quad (27)$$

Since X_α are known, $dX_\alpha = 0$. Also

$$de = e - e^{n-1}, \quad dv = v - v^{n-1}, \quad (28)$$

where

$$e^{n-1} = e(p^{n-1}, T^{n-1}, X_\alpha), \quad v^{n-1} = v(p^{n-1}, T^{n-1}, X_\alpha) \quad (29)$$

are computed from the EOS. The needed derivatives can be calculated from C_p , κ_T and α_v (where h, e in J/kg, C_p, C_v in J/mol K) as

$$\left(\frac{\partial T}{\partial v} \right)_{e, X_\alpha} = \frac{1}{v \alpha_v} \left(1 - \frac{C_p}{C_v} \right) + \frac{p}{C_v}, \quad \left(\frac{\partial T}{\partial e} \right)_{v, X_\alpha} = \frac{m}{C_v}, \quad (30)$$

$$\left(\frac{\partial p}{\partial v}\right)_{e,X_\alpha} = \frac{1}{\kappa_T} \left(-\frac{C_p}{C_v} \frac{1}{v} + \alpha_v \frac{p}{C_v}\right), \quad \left(\frac{\partial p}{\partial e}\right)_{v,X_\alpha} = \frac{m}{C_v} \frac{\alpha_v}{\kappa_T}. \quad (31)$$

The iteration is conducted by updating (p, T) until de and dv are within a desired tolerance, e.g. $de/e < 10^{-6}$, $dv/v < 10^{-6}$. The initial guess for (p, T) is from the previous time step, or the previous Runge-Kutta stage. For the O_2/H_2 regime under consideration, (p, T) converge in 2 iterations. It was also noted that if the initial guess for (p, T) is $(p_\infty, (T_1 + T_2)/2)$, 4 or 5 iterations are required for convergence. Thus, there appears to be no need to store (p, T) , therefore relaxing some of the computation overhead associated with this iteration. In fact, the memory overhead of the iterative method is the addition of the four arrays necessary to store e, v, e^{n-1}, v^{n-1} . Compared with the heptane/nitrogen simulations where a PR EOS for computing the pressure and an energy fit for temperature were employed [9], here an additional 50% CPU time per time step is used. However, for the O_2/H_2 mixture, the form of the energy fit for the temperature would be considerably more complicated than that of the heptane/nitrogen mixture, and the pressure can no longer be computed directly from the molar volume.

6.3 Resolution

The appropriate resolution of all scales is checked by visual inspection of the dilatation field, $\nabla \cdot u$, which is the most sensitive to numerical errors. The absence of small scale fluctuations in $\nabla \cdot u$ is well known to be a reasonable indicator of good resolution.

Generally, the flow field is extremely sensitive to having an appropriate resolution, and its lack is manifested by the code crashing. Another diagnostic of inadequate resolution is an increasing number of iterations for the convergence of the calculation involving the EOS, leading eventually to the code crashing as well.

7 Initial conditions

The appropriate initial conditions for simulating the evolution of mixing layers are notoriously difficult to choose, especially for density stratified situations (see a discussion in Miller et al. [8]). To this end, following Drazin and Reid [19], there are two issues that must be addressed: first, one must inquire about the basic (i.e. mean) flow, and then about the appropriate disturbance. Both of these issues were thoroughly investigated by Okong'o and Bellan [21] for real gases, and applied to the heptane/nitrogen system under supercritical conditions. The same formalism is applied here to explore the specific features of the O_2/H_2 system. Having determined here (by numerically solving the laminar equations) that the form of the basic flow for the O_2/H_2 system is that of an errorfunction-like profile (not shown), and thus that it has a single inflection point, a two-dimensional stability analysis is performed with the error function representing the mean flow; this is acceptable since according to

Drazin and Reid [19], for mean flows displaying a single inflection point the stability analysis is not sensitive to the exact form of the mean flow.

The freestream velocity is specified as

$$\bar{u}_1(\infty) = U_1; \quad \bar{u}_1(-\infty) = U_2 \quad (32)$$

and the mean velocity, temperature and mass fraction follow an error function profile, as listed below. Since the pressure is constant, the speed of sound and inverse of the density also assume approximately error function profiles. Therefore, the profiles used in the stability analysis are

$$\bar{u}_1(x_2) = \bar{u}_1(-\infty) + \frac{[\bar{u}_1(\infty) - \bar{u}_1(-\infty)]}{2} \left[\operatorname{erf} \left(\sqrt{\pi} \frac{x_2}{\delta_\omega} \right) + 1 \right], \quad (33)$$

$$a_s(x_2) = a_s(-\infty) + \frac{[a_s(\infty) - a_s(-\infty)]}{2} \left[\operatorname{erf} \left(\sqrt{\pi} \frac{x_2}{\delta_\omega} \right) + 1 \right], \quad (34)$$

$$\frac{1}{\bar{\rho}(x_2)} = \frac{1}{\bar{\rho}(-\infty)} + \frac{1}{2} \left[\frac{1}{\bar{\rho}(\infty)} - \frac{1}{\bar{\rho}(-\infty)} \right] \left[\operatorname{erf} \left(\sqrt{\pi} \frac{x_2}{\delta_\omega} \right) + 1 \right]. \quad (35)$$

Several mean flow conditions are listed in Tables 2 - 4. To find the stability characteristics of the layer, perturbations are imposed through

$$\Delta u_i = \hat{u}_i(x_2) \exp[i\alpha(x_1 - ct)], \quad (36)$$

$$\Delta p = \hat{p}(x_2) \exp[i\alpha(x_1 - ct)], \quad (37)$$

$$\Delta \rho = \hat{\rho}(x_2) \exp[i\alpha(x_1 - ct)], \quad (38)$$

where α is real and c is complex, and the hat denotes the perturbation amplitudes, all of which are functions of x_2 only. Within the protocol of the stability analysis, the physical quantities are obtained by taking the real part (subscript *re*) of the complex quantities.

Since the mean velocity, density and speed of sound have the same profiles as for heptane-nitrogen [21], the stability curves could be expected to be similar for the same initial density stratification and $M_{c,0}$. However, as illustrated in Fig. 2a where results are obtained for the conditions listed in Tables 2 and 3, discrepancies arise because, due to the different fluid properties, the freestream Mach numbers are different. Generally, the most unstable wavelengths are slightly longer for the O_2/H_2 mixture, as can be seen from Fig. 2a and from a comparison of Table IV in [21] with Table 5 herein, listing the most unstable wavelengths. More important and directly relevant to the strategy of conducting simulations for temperature ratios

$|T_2 - T_1|/T_2$ as large as possible, even for values of $|T_2 - T_1|/T_2$ quite smaller than unity, ρ_2/ρ_1 is here very large, and certainly much larger than for heptane/nitrogen. Equivalently, as listed in Table I of [21] and Table 3 herein, $\rho_2/\rho_1 = 12.88$ corresponds to $|T_2 - T_1|/T_2 = 0.667$ for heptane/nitrogen and 0.2 for O_2/H_2 , while $|T_2 - T_1|/T_2 = 0.5$ returns $\rho_2/\rho_1 = 24.40$ for O_2/H_2 as shown in Table 4. For smaller freestream temperatures and $|T_2 - T_1|/T_2 = 0.5$, the stratification is even larger, as shown in Fig. 2c for a range of T_1 and T_2 and at $p = 100$ and 400 atm. This indicates that as ρ_2/ρ_1 becomes larger, due to computational constraints associated with an increased number of nodes in the direction of the initial density gradient stratification (i.e. x_2) for the same resolution, the O_2/H_2 DNS must be restricted to smaller ratios $|T_2 - T_1|/T_2$ than the equivalent simulations conducted for heptane/nitrogen [9], [21]. Therefore, all simulations conducted herein will be for the mean flow properties displayed in Table 4, and only Re_0 will be varied.

Following the arguments of Okong'o and Bellan [21] showing that 3D eigensolutions to the stability problem are not uniquely defined, the simulations are started with heuristic streamwise and spanwise vorticity perturbations [20],[22] superimposed on the mean initial velocity profile

$$\omega_1(x_2, x_3) = F_{3D} \frac{\lambda_1 \Delta U_0}{\Gamma_1} f_2(x_2) f_3(x_3) \quad (39)$$

$$\omega_3(x_1, x_2) = F_{2D} \frac{\lambda_3 \Delta U_0}{\Gamma_3} f_1(x_1) f_2(x_2) \quad (40)$$

where Γ_1 and Γ_3 are the circulations,

$$f_1(x_1) = A_0 \left| \sin \left(\frac{\pi x_1}{\lambda_1} \right) \right| + A_1 \left| \sin \left(\frac{\pi x_1}{2\lambda_1} \right) \right| + A_2 \left| \sin \left(\frac{\pi x_1}{4\lambda_1} \right) \right| + A_3 \left| \sin \left(\frac{\pi x_1}{8\lambda_1} - \frac{\pi}{2} \right) \right| \quad (41)$$

$$f_2(x_2) = \exp \left[-\pi \left(\frac{x_2}{\delta_{\omega,0}} \right)^2 \right] \quad (42)$$

$$f_3(x_3) = B_0 \sin \left(\frac{2\pi x_3}{\lambda_3} \right) + B_1 \sin \left(\frac{\pi x_3}{L_3} \right). \quad (43)$$

We use $F_{2D} = 0.1$, $A_0 = 1$, $A_1 = 0.5$, $A_2 = A_3 = 0.35$ for the streamwise perturbations, and $F_{3D} = 0.05$, $B_0 = 1$ and $B_1 = 0.025$ for the spanwise perturbations. The wavelength of the perturbation is $\lambda_1 = 7.29\delta_{\omega,0}$ (the most unstable wavelength for incompressible flow) and $\lambda_3 = 0.6\lambda_1$, following [20]. Since this perturbation wavelength is smaller than the most unstable one, $\lambda_1 = 10.35\delta_{\omega,0}$, and the difference between the

two values is significant, based on the results of Okong'o and Bellan [21] with simulations perturbed at wavelengths smaller than the most unstable one, it is expected that even if a transitional state is here achieved, the structures will not be as convoluted as when the layer would be perturbed with the most unstable wavelength. The initial vorticity thickness $\delta_{\omega,0}$ is 6.859×10^{-3} m. The grid is chosen for all simulations so as to accommodate four wavelengths in the streamwise and spanwise directions, and the evolution of the layer is meant to encompass rollup and two pairings of the initial spanwise vortices. For these initial conditions, the grid sizes and the resolutions are displayed in Table 6.

8 Results

The results of the simulations listed in Table 6 are here discussed. For the first simulation, the value of Re_0 is chosen to be 600 to emulate a condition which led to a transitional state for the heptane/nitrogen mixing layer studied by Okong'o and Bellan [9]; however, that mixing layer had an initial density stratification of 12.88 instead of the much larger value of 24.40 employed in the present study. The larger $Re_0 = 750$ of the second simulation represents an effort to enhance the probability of reaching a transitional state; however, this more elevated Re_0 did not lead to transition either. To understand the physics associated with these results, we first focus on the global characteristics of the layer with special emphasis on the features indicative of transition. Further, we investigate the specific aspects of the instantaneous fields which are inherently absent from the measures given by the global characteristics. Finally, in order to understand some of the peculiarities of the instantaneous fields, we conduct a second order statistical analysis focussing on the dissipation.

8.1 Global growth characteristics

One of the essential characteristics of a mixing layer is its growth. Although many definitions of growth appear in the literature, Cortesi et al. [23] showed that several such measures, including the momentum thickness, are qualitatively similar. Here, we define the momentum thickness as

$$\delta_m = \frac{-1}{(\theta_1 - \theta_2)^2} \int_{-L_{2,\min}}^{L_{2,\max}} (\theta_2 + \langle \rho u_1 \rangle)(\theta_1 + \langle \rho u_1 \rangle) dx_2 \quad (44)$$

with $\theta_1 = \langle \rho u_1 \rangle_{x_2=L_{2,\max}}$ and $\theta_2 = \langle \rho u_1 \rangle_{x_2=L_{2,\min}}$, where $L_{2,\min} = -L_2/3$ and $L_{2,\max} = 2L_2/3$. While the growth is mostly a consequence of entrainment, the product thickness defined as $\delta_p = \int \int \int_V \rho Y_p dV$ in mass units, where $Y_p = 2 \min(Y_O, Y_H)$, is a direct consequence of molecular mixing as also explained by Cortesi et al. [23]. Both of these quantities, non-dimensionalized, are illustrated versus the nondimensional time $t^* = t\Delta U_0/\delta_{\omega,0}$ in Fig. 3a, respectively, for the R600 and R750 simulations. The non-dimensional momentum thickness, $\delta_m/\delta_{\omega,0}$ of both layers is similar.

The R600 layer exhibits the first pairing at $t^* = 80$, but does not show promise of a second pairing by $t^* = 125$, at which time the simulation was terminated due to lack of further interest. In comparison, the R750 layer pairs first at $t^* = 80$ and finishes the second pairing at $t^* = 150$; this simulation was continued to $t^* = 190$ to explore the possible transition to turbulent mixing after the second pairing. Despite the continuous growth of the layer, and the attainment of a relatively large $Re_m = 1680$, the R750 layer does not reach transition for reasons discussed below. Compared to other initially density stratified layers such as drop laden layers (c.f. Miller and Bellan [24]; stratification of 1.5), or to supercritical layers of lesser initial stratification (c.f. Okong'o and Bellan [9]; stratification of 12.88), the present layers do not show the characteristic $\delta_m/\delta_{\omega,0}$ plateaux indicative of the influence of the forcing. This fact is attributed to the much larger present stratification, resulting in a resistance to entrainment. The nondimensional product thickness, $\delta_p/\delta_{p,0}$, displays a continuous growth indicating that despite the lack of transition, molecular mixing proceeds unabated.

Depicted in Fig. 3b are rotational global features of the layers: the non-dimensional positive spanwise vorticity, $\langle\langle \omega_3^+ \rangle\rangle (\delta_{\omega,0}/\Delta U_0)$, and the non-dimensional enstrophy, $\langle\langle \omega_i \omega_i \rangle\rangle (\delta_{\omega,0}/\Delta U_0)^2$, where $\omega = \nabla \times \mathbf{u}$ is the vorticity; here $\langle\langle \rangle\rangle$ denotes volume averaging. Since the initial mean velocity profile is such that the initial spanwise vorticity is negative, $\langle\langle \omega_3^+ \rangle\rangle (\delta_{\omega,0}/\Delta U_0)$ is an indicator of the development of small turbulent scales. Complementing this information, $\langle\langle \omega_i \omega_i \rangle\rangle (\delta_{\omega,0}/\Delta U_0)^2$ is a manifestation of stretching and tilting, the mechanism which is primarily responsible for the formation of small scales. For both simulations, $\langle\langle \omega_3^+ \rangle\rangle (\delta_{\omega,0}/\Delta U_0)$ increases from the null value once the layer rollup is completed; however, a reduced augmentation rate is displayed by the R600 simulation corresponding to the reduced layer growth. The peak in the curve portraying the R600 simulation, and the first peak in the corresponding curve for the R750 simulation occur at the first vortex pairing. Another peak, but of smaller magnitude is displayed by the R750 layer at the time station of the second pairing; the relative magnitude of these two peaks is a first indication of lack of mixing transition. Supporting evidence of lack of mixing transition evolves from examining the $\langle\langle \omega_i \omega_i \rangle\rangle (\delta_{\omega,0}/\Delta U_0)^2$ plots. The increase in enstrophy of the R600 is sporadic and modest, with two equivalent magnitude peaks evident at rollup and first pairing; past the first pairing, the enstrophy decays beyond its value at the initial condition. In contrast to the R600 results, for R750 the enstrophy culminates, with a substantial peak, at the first vortex pairing; subsequently, the plot displays a decay supporting the lack of transition. According to the detailed discussion in Okong'o and Bellan [21] analyzing the reasons for lack of transition in temporal mixing layers, in the R750 simulation we witness the early formation of substantial small turbulent scales which destroy the coherence of the vortices, thus impeding entrainment, pairing and further development of turbulent scales.

The analysis presented below is to ascertain that this physical picture is correct

and complete.

8.2 Vorticity production

To explore the global rotational state of the R750 layer, we examine the budget of the spanwise vorticity in the $(x_1 - x_3)$ homogeneous planes, and inspect both the average and the RMS. A parallel examination is conducted for the vorticity magnitude squared.

The vorticity equation for a compressible flow is

$$\frac{D\omega}{Dt} = (\omega \cdot \nabla)\mathbf{u} - (\nabla \cdot \mathbf{u})\omega - \nabla\left(\frac{1}{\rho}\right) \times \nabla p + \nabla \times \left(\frac{1}{\rho} \nabla \cdot \bar{\tau}\right) \quad (45)$$

where D/Dt is the substantial derivative, and the equivalent equation for the vorticity magnitude squared follows

$$\frac{D(\omega^2)}{Dt} = 2\omega \cdot (\omega \cdot \nabla)\mathbf{u} - 2(\nabla \cdot \mathbf{u})\omega^2 - 2\omega \cdot \nabla\left(\frac{1}{\rho}\right) \times \nabla p + 2\omega \cdot \nabla \times \left(\frac{1}{\rho} \nabla \cdot \bar{\tau}\right). \quad (46)$$

The first term in eqs. 45 and 46 represents the stretching and tilting contribution, the second term describes the effect of dilatation, the third term is the baroclinic participation to vorticity production, and the last term portrays the viscous contribution. Depicted in Figs. 4a and 4b are the non-dimensional average and RMS of the spanwise vorticity budget at $t^* = 80$, corresponding to the end of the first pairing. Most of the spanwise rotational activity of the layer, both average and RMS, is located in the H_2 side, where the lighter fluid is situated. The average spanwise vorticity budget is dominated by large peaks of the viscous term, while at some locations the stretching and tilting term competes with the viscous term. On the LOX side of the layer, the activity is dominated by the baroclinic term, while the positive dilatation contribution rivals in magnitude the negative stretching and tilting term. Compared to the average spanwise vorticity, the RMS displays a large culmination of the stretching and tilting term at the boundary between the two species, indicating that in this crucial region of small scale formation there is a considerable activity, explaining the large enstrophy peak at this time station. On the H_2 side of the layer, stretching and tilting and viscous terms contribute similarly to the RMS and dominate the dilatation and baroclinic term; on the LOX side of the layer, the viscous term dominates, although there is appreciable activity in all other terms. The indication is that in the LOX side, the formed turbulent scales are dissipated by the action of viscosity. The result of this dissipation is clearly seen in Figs. 4c and 4d, showing the non-dimensional average and RMS of the vorticity magnitude squared budget; the viscous term is larger in magnitude than all other terms, and negative while the second term in order of decreasing magnitude is the stretching and tilting term, which is positive thus indicating production of vorticity by this mechanism. Production through all mechanisms is negligible in the LOX side of the layer, and the

insignificant amount produced is dissipated by the dominating viscous effect. Finally, the RMS of the vorticity magnitude budget depicts the same ordering of terms as the RMS of the spanwise vorticity budget.

To understand the timewise evolution of the layer, illustrated in Figs. 5a and 5b are the non-dimensional average and RMS of the spanwise vorticity budget at $t^* = 150$. Similar to the $t^* = 80$ situation, most of the spanwise rotational activity of the layer, both average and RMS, is located on the H_2 side. Compared to the magnitude of the equivalent terms at $t^* = 80$, all terms are here reduced approximately by a factor of 2, indicating that vorticity production is abated; this finding is totally consistent with the global characteristics presented above. The dominant contribution to the average spanwise vorticity is from the stretching and tilting term which is negative, although at some cross-stream locations situated well into the H_2 side of the layer the viscous term rivals the stretching/tilting one in magnitude, and is positive. Both the averaged dilatation and baroclinic terms appear much smaller. This ordering of the relative magnitudes is even more dramatic in the RMS budget. Clearly, the RMS production is primarily due to stretching/tilting and viscosity effects which are essentially of similar magnitude; dilatation and baroclinic influences are smaller by approximately a factor of 4. In Figs 5c and 5d, a similar evaluation is presented for the vorticity magnitude squared. Although generally the same ordering of stretching/tilting and viscosity versus dilatation and baroclinic terms holds, viscous effects dominate the stretching/tilting activity, and the average viscous contribution seems to extend further into the LOX side of the layer. As expected, stretching/tilting is responsible for increasing the magnitude of the vorticity squared due to production of small scales, whereas the viscous term diminishes the magnitude of the vorticity through dissipation. The physical picture emerging is that production of small scales does not keep up with dissipation, therefore preventing the layer from reaching a transitional mixing state.

The analysis presented below is devoted to (i) corroboration of the above-derived conclusions based on the global characteristics and vorticity budgets of the layer at important time stations, (ii) a documentation of the specific aspects of LOX/ H_2 mixing layers in the thermodynamic regime chosen herein, and (iii) an in-depth inquiry into the reasons responsible for the lack of transition. The R750 database is examined exclusively, but the conclusions pertain to the R600 simulation as well.

8.3 Visualizations of the dynamic and thermodynamic variables

Instantaneous aspects of the flow may reveal information that is unavailable from global characteristics. Such instantaneous aspects are best illustrated through contour plots at specific times and locations, chosen so as to highlight important features of the layer. Since two important times are $t^* = 80$ and 150, as explained above, the flow visualizations will depict the variables at one or both of those times.

Dynamic variables As discussed above, one of the most fundamental variables indicating the evolution of the flow is the spanwise vorticity. Shown in Figs. 6a and 6b are braid cross-section ($x_3 = L_3/16 = 0.0075$ m) distributions of the spanwise vorticity at $t^* = 80$ and 150, respectively; the between-the-braid plane cross-sections ($x_3 = L_3/2 = 0.06$ m) display an equivalent behavior. At $t^* = 80$, the two vortices remaining after the second pairing are clearly shown, whereas at $t^* = 150$ only a single vortex appears; however, some remnants of the second pairing process are obvious. The level of the positive spanwise vorticity, indicative of small scale formation decreases from $t^* = 80$ to 150, consistent with the global peak in positive spanwise vorticity as a function of time; however, the maximum positive spanwise vorticity increases in the between-the-braid plane as the layer evolves from the first to the second pairing. Noteworthy is the irregular, ‘collapsed’ aspect of the single vortex, similar to other such single vortices resulting from two pairings in simulations that did not achieve transition (see Okong’o and Bellan [21]). This is due to the early small scale formation induced by the relatively large value of F_{3D} , and results in the destruction of coherence of the vortex, impeding entrainment which is the crucial ingredient to growth.

The evolution of the streamwise vorticity in the mid-braid plane was documented by many investigators for gases at atmospheric conditions (e.g. Rogers and Moser [25]). Of particular interest for qualitative comparison with the present results are the plots of Cortesi et al. [27] for gravitationally density-stratified temporal mixing layers; for such layers, the influence of gravity is measured by the value of the Richardson number. Presented in Figs. 7a and 7b are the present streamwise mid-braid plane ($x_1/\delta_{\omega,0} = 25.6$) contours at $t^* = 80$ and 150, respectively. These instantaneous plots may be compared with those in Figs. 9a and 9b of Rogers and Moser [25] corresponding to time stations after the first and second pairings, respectively. Both in Figs. 7a and 7b, distortions are observed in the cross-stream direction when comparing with the equivalent figures in [25] which display a definite symmetry. This symmetry of the structures both in the cross-stream and the spanwise direction no longer exists here due to the initial layer density stratification. The overwhelming activity is in the H_2 side of the layer, containing the lighter fluid. On the other hand, comparisons with Fig. 16a of Cortesi et al. [27] show that their streamwise vorticity also lacks symmetry; however, those calculations are not quantitatively comparable with ours because of the different forcing, among other different aspects. For example, Cortesi et al. [27] find that as the Richardson number is increased, the structures recover some symmetry (their Fig. 17a).

Thermodynamic variables In previous studies of supercritical mixing layers [8], [9], [21] for heptane/nitrogen at 60 atm and freestream temperatures of $T_1 = 1000$ K and $T_2 = 600$ K, the peculiarities of the layer were associated with departures from perfect gas behavior ($Z = 1$ for a perfect gas), and departures from mixture ideality (for an ideal mixture $\alpha_D = 1$). These associations were issued from quantitative as

well as visual correlations. Contour plots of Z and α_D for the present LOX/ H_2 layer (freestream conditions of 100 atm, $T_1 = 600$ K and $T_2 = 400$ K) at different time stations, both in the braid and in the between-the-braid planes reveal that the fluid is extremely close to a perfect gas and the mixture is nearly ideal. For example, at $t^* = 150$ the compression factor varies between 1.009 and 1.035, whereas the mass diffusion factor varies between 0.9939 and 0.9996. Therefore, none of the features discussed below can be associated with specific real gas or non-ideal mixture behavior. It should, however, be noted that this thermodynamic state of the layer could not be foreseen *a priori*, and it is only a result of the calculation. (Moreover, it is expected that at the same pressure, with decreasing temperatures the mixture will increasingly exhibit departures from perfect gas and ideal mixture conditions.)

One of the most distinctive features of supercritical mixing layers examined so far is the existence of regions of high density-gradient magnitude (called further herein by the acronym HDGM). These regions have been identified in both pre-transitional [8], [21] and transitional [9], [21] supercritical mixing layers. Given the perfect gas and near ideal conditions of this layer, in retrospect these distinctive features could perhaps be better associated with the initial density stratification. However, movie animations of the $|\nabla\rho|$ timewise evolution show that the origin of these regions is not only from the distortion of the initial boundary between the two fluid species, but also from the mixing between the two species; this conclusion holds for all supercritical mixing layers studied so far, independent of the binary system of species. Illustrated in Figs. 8a and 8b is $|\nabla\rho|$ in the braid and the between-the-braid cross-sections located at $x_3 = 0.0075$ m and $x_3 = 0.06$ m, respectively, at $t^* = 150$. Compared to heptane/nitrogen mixing layers excited at the same wavelength and F_{3D} [9], the present regions of high $|\nabla\rho|$ are less convoluted and each such structure is more spread-out, particularly in the between-the-braid plane. The decreased convolution is the result of both lack of transition and the fact that the excitation wavelength is here further away from the most unstable wavelength found in the stability analysis (see Figs. 2a and 2b). The fact that each of the HDGM structures is more spread-out is attributed to the increased solubility in the LOX/ H_2 system with respect to the heptane/nitrogen one. For example, in studies of heptane drops in nitrogen, Harstad and Bellan [14] found that the initial density discontinuity is maintained, although the location of the discontinuity changes during the drop evolution. In contrast, a LOX drop in H_2 displays a quicker relaxation of Y_O from unity inside the drop, indicating important H_2 solubility effects (see Harstad and Bellan [16]).

Since the existence of the HDGM regions cannot be here associated with real gas effects, or entirely due to the initial density stratification, the question arises as to their origin. Clearly, they are the result of mixing, without which they would not be formed. Parcels of heavy LOX are entrained into the lighter H_2 and they lose their identity only after mixing at the small scale. Before that time, the much larger molar weight of O_2 gives rise to a substantial density gradient. Therefore, the HDGM regions are here attributed to the very large molar weight ratio (a factor of

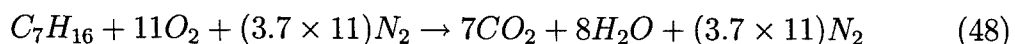
16) between O_2 and H_2 . Contrary to the situation encountered for heptane/nitrogen where diffusion (which is a molecular scale process) was inhibited by the lower than unity mass diffusion factor, here such diffusion is efficient ($\alpha_D \sim 1$). Thus, we find that generally, HDGM regions may occur under quite different circumstances. For large molar weight ratio species, these regions may occur even if the species diffuse well (and we note again that this is a molecular scale process). For species having a modest to low molar weight ratio, HDGM regions may still occur if the species have difficulty in diffusing into each other.

To investigate the visual correlation between the HDGM regions and the distribution of Y_O , contour plots of the LOX mass fraction at $t^* = 150$ are displayed in Fig. 9a and 9b representing the braid and the between-the-braid planes. As inferred above, some parcels of LOX have broken off from the lower stream and are seen convected to the upper stream. Also, the layer consists of substantially inhomogeneous fluid composed of both LOX and H_2 . An equivalent physical picture of non-homogeneities is obtained when examining the Y_O distribution at $t^* = 150$ in the streamwise mid-braid plane located at $x_1/\delta_{\omega,0} = 25.6$, shown in Fig. 9c. The characteristic ‘mushroom’ shapes typical of the streamwise plane of 3D simulations are evident; equivalent $|\nabla\rho|$ contours (not shown) are found. The disintegration of the lower O_2 stream and the migration of parcels of O_2 into the H_2 stream are manifest. Noteworthy, Cortesi et al. [23] also detected these mushroom structures (their Fig. 9a) evolving during the simulation of gravitationally density-stratified 3D mixing layers forced deterministically. These structures were less developed when a combined deterministic-random velocity field was used during the initialization.

To quantitatively assess the composition of the HDGM regions, conditional averages are listed in Table 7 representing the spatial distributions at $t^* = 150$; a similar calculation performed at $t^* = 80$ yielded similar results up to the third digit. The conditional averages are calculated over regions of $|\nabla\rho| > |\nabla\rho|_{cutoff} \equiv K |\nabla\rho|_{\max}$ with $K = 0.1, 0.2, 0.3$ and 0.4 . As higher values of $|\nabla\rho|$ are probed, the mass fraction of LOX increases, similarly to the findings with the heptane/nitrogen system [9]; however, for the same cutoff constant, the average mass fraction values are here higher. Nevertheless, because of the large ratio of O_2/H_2 molar weights, the average Y_O seems closer to stoichiometric than could be inferred for the heptane/nitrogen simulation for which directly equivalent evaluations are not possible owing to the lack of O_2 in the mixing layer simulations. Considering that the stoichiometric O_2 mass fraction is here $Y_{O,s} = 32/(32 + 4) = 0.89$, being calculated from the reaction



the present values of 0.906 to 0.956 found from conditional averages seem to indicate a globally favorable situation for combustion purposes. In contrast, for heptane/air the stoichiometric heptane mass fraction calculated from the reaction



is $Y_{h,s} = 100/(11 \times 32 + 3.7 \times 11 \times 28) = 0.067$, which compares less favorably with values of 0.84 to 0.921 found from similar conditional averages with $K = 0.1, 0.2$ and 0.3 using the results of a heptane/nitrogen simulation[9]. This comparison is only qualitatively correct since the simulations in [9] were based on the heptane/nitrogen instead of the heptane/air system.

To further assess the correlation between $|\nabla\rho|$ and Y_O , listed in Table 8 are the global coefficients found in the braid and the between-the-braid planes at $t^* = 150$. The volume based correlation between two variables is defined by

$$\mathcal{R}_2(\mathcal{X}, \mathcal{Y}) = \frac{\langle\langle \mathcal{X}\mathcal{Y} \rangle\rangle - \langle\langle \mathcal{X} \rangle\rangle\langle\langle \mathcal{Y} \rangle\rangle}{\sqrt{(\langle\langle \mathcal{X}^2 \rangle\rangle - \langle\langle \mathcal{X} \rangle\rangle^2)(\langle\langle \mathcal{Y}^2 \rangle\rangle - \langle\langle \mathcal{Y} \rangle\rangle^2)}} \quad (49)$$

where \mathcal{X} and \mathcal{Y} are generic variables. The correlation in Table 8 is moderate and similar to that found in a previous study for heptane/nitrogen.

Because the temperature is directly related to the density through the EOS, the expectation is that the temperature distribution will be visually highly correlated with $|\nabla\rho|$ if the pressure is approximately constant. Indeed, examination of pressure contours in both the braid and the between-the-braid planes (not shown) reveals that the variations from the initial uniform pressure are small, at most 8%. Consistent with the almost uniform pressure, the braid and the between-the-braid temperature contours shown in Figs. 10a and 10b are visually well correlated with $|\nabla\rho|$. Hotter fluid from the upper stream is transported to the lower stream, and the HDGM regions generally contain fluid at higher temperature than their surroundings. This situation is very beneficial to combustion since it has been determined above that in these regions the composition is close to stoichiometric.

8.4 Irreversible entropy production (dissipation)

Okong'o and Bellan [10] have analyzed the reasons for the lack of transition in 3D supercritical heptane/nitrogen mixing layers, and found that it is due to the HDGM regions which acted similar to material surfaces and damped small turbulent scales formed through stretching and tilting. This conclusion was derived from an irreversible entropy production analysis (the irreversible entropy production is in fact the dissipation). Specifically, if Σ_j represents the reversible flux of entropy and g denotes the rate of irreversible entropy production, then

$$\Sigma_j = (q_{IK,j} - \mu_O j_{Oj}/m_O - \mu_H j_{Hj}/m_H) / T \quad (50)$$

where μ_H and μ_O are the chemical potentials (partial molar Gibbs free energy), $j_{Hj} = -j_{Oj}$, and g is the sum of viscous, Fourier heat flux and molar flux contributions

$$g = g_{visc} + g_{temp} + g_{mass}, \quad (51)$$

$$g_{visc} = \frac{\mu}{T} (2S_{ij}S_{ij} - \frac{2}{3}S_{kk}S_{ll}), \quad g_{temp} = \frac{\lambda}{T^2} \frac{\partial T}{\partial x_j} \frac{\partial T}{\partial x_j}, \quad g_{mass} = \frac{1}{Y_H Y_O \rho D} \frac{R_u m}{m_H m_O} j_{Oj} j_{Oj}, \quad (52)$$

$$S_{ij} = \frac{1}{2} \left(\frac{\partial u_i}{\partial x_j} + \frac{\partial u_j}{\partial x_i} \right), \quad (53)$$

where according to eqs. 6 - 8, g_{mass} contains the departure from mixture non-ideality (through j_{Oj}), $\propto \alpha_D$, and the Soret term, $\propto \alpha_{BK}$. One of the important issues determined was the contribution of each of the terms listed in eq. 52 to g , from $(x_1 - x_3)$ plane averages considering both the average and RMS, as well as an equivalent evaluation from volume averages. Analysis of the data at three time stations located before, at and after the culminating point of the global positive spanwise vorticity showed that whereas at all times the primary contribution to volume averages was from g_{visc} . At the time following the culminating global positive spanwise vorticity, visualizations showed that most of the g , as well as the g_{visc} and g_{mass} activity was concentrated at HDGM locations. This dissipation mechanism was considered responsible for the lack of transition, as formed small scales were damped by the region of large $|\nabla\rho|$ which acted similar to a material interface. These conclusions were consistent with those of Hannoun et al. [26] who experimentally investigated the turbulence structure near a sharp density interface.

A similar analysis was performed by Okong'o and Bellan [9] for a transitional supercritical heptane/nitrogen mixing layer, with somewhat different results. One of the important results was that the visual correlation between g and HDGM locations no longer existed.

Similarly to our previous work, we use here the inspection of the dissipation as a diagnostic determining the causes of the lack of transition. To this end, illustrated in Figs. 11a and 11b are the braid and the between-the-braid plane distributions of g at $t^* = 150$, respectively. A visual comparison with the $|\nabla\rho|$ plots of Figs. 8a and 8b leads to the conclusion that there is a lack of correlation between these two quantities. While there are some regions of common activity, few regions of very large dissipation correspond to locations of HDGM. The regions of highest g and $|\nabla\rho|$ activity are even more separated at $t^* = 80$. The difference between the present situation and that studied by Okong'o and Bellan [10] for heptane/nitrogen is that here the density stratification is much larger, inhibiting the formation of small scales in the LOX side of the layer. This explanation is supported by the vorticity budget analysis conducted above where the lack of activity of the crucial stretching and tilting term on the LOX side of the layer was noted, and by the striking visual lack of correlation between g and HDGM locations. In contrast, in [10] small scales were formed on the heptane side, but they were being damped by the action of viscosity in the HDGM regions.

Homogeneous-plane average plots of the g_{visc} , g_{mass} and g_{temp} contributions to g displayed in Figs. 12a (average) and 12b (RMS) at $t^* = 150$ are typical of the

situation at $t^* = 80$ as well. Contributions from g_{mass} and g_{temp} effects are about two orders of magnitude smaller than viscosity effects and this holds for both the average and the RMS. Consistent with the discussion on the lack of correlation between g and the HDGM regions which are primarily located in the LOX side of the layer, here the viscous activity is considerably stronger on the H_2 side of the layer, where the lighter fluid is located; this is true for both the average and the RMS. On the other hand, the dissipation due to the molar fluxes is stronger on the LOX side of the layer where the mass fraction and temperature gradients are larger. Finally, the much smaller g_{temp} is the result of the enhanced Le_{eff} at supercritical conditions, as shown by Harstad and Bellan [11]. The larger Le_{eff} causes the temperature to relax faster than the mass fraction (non-dimensional gradients are smaller), as the larger (than at low pressure conditions) thermal conductivity promotes heat transfer.

Based on this analysis, the lack of transition is due to two combined effects. Small scales are formed excessively early in the evolution of the layer, destroying the coherence of the ultimate vortex; this was elucidated by inspecting the global characteristics of the layer, by evaluating the vorticity and vorticity magnitude budgets, and by examining visualizations of the spanwise vorticity. As a result of the weakened vortex, entrainment is reduced and the small scales cannot develop. This effect is enhanced by the very large stratification which further prevents the formation of small scales. Evidence for this latter effect is found from exploring the development of the dissipation and its main contributions, as well as by scrutinizing visualizations of the dissipation and the density gradient magnitude.

9 Summary and conclusions

A Direct Numerical Simulation study has been performed of a three-dimensional temporal LOX/ H_2 mixing layer in order to explore aspects of LOX disintegration under shearing conditions. The conservation equations were based on fluctuation-dissipation theory, having an enlarged transport matrix that includes Soret and Dufour effects. To close the system of equations, a real gas equation of state was coupled to the differential equations. Transport properties were accurate as much as possible in the chosen (p, T) regime to ensure the resolution of the Batchelor scales. This was accomplished by correlating the Schmidt and Prandtl numbers as functions of the thermodynamic variables, consistent with contour plots of these numbers based on accurate properties. The values of these numbers determined the thermal conductivity and diffusivity, while the viscosity was determined from the prescribed initial value of the Reynolds number. Boundary conditions were of periodic type in the streamwise and spanwise directions, and of outflow type, based on a real gas characteristic analysis of the differential equations, in the cross-stream direction. Additional to the Reynolds number, the initial conditions prescribed the Mach number, the temperatures of the two freestreams, the pressure, and the perturbation of the layer.

A stability analysis conducted for the O_2/H_2 system showed that at the same

density stratification, the stability curve is similar to the heptane/nitrogen system previously studied. However, at the enlarged stratifications characteristic of thermodynamic regimes of interest for the O_2/H_2 system, the density stratification is much larger and the most unstable wavelength is longer. It is shown that at high pressure, as the oxygen is at lower temperatures, the stratification increases dramatically.

Based on the stability analysis and previous experience with heptane/nitrogen supercritical mixing layers, the perturbation wavelength was chosen to be the most unstable incompressible one, and the amplitudes of the excitation were those that previously lead to transition in a similar heptane/nitrogen mixing layer simulation having albeit a smaller initial density stratification. The domain size was four times the perturbation wavelength to accommodate four vortices and two pairings. Two mixing layer conditions were simulated differing only by the initial Reynolds number. As the simulations are very computationally intensive, one simulation was pursued only past the first pairing, as it was obvious that transition would not be obtained. The second simulation, at a larger initial Reynolds number, evolved through two pairings, but also did not reach transition. To determine the causes leading to the lack of transition, a detailed analysis of the layer was conducted.

Global characteristics of the layer showed a momentum thickness and product thickness continuous growth, with a relatively large momentum thickness based Reynolds number reached. However, these aspects were not sufficient to induce transition. The evolution of the global positive spanwise vorticity and the enstrophy displayed a large peak following the first pairing, and continued to decay afterwards with only a minor increase following the second pairing. This information, interpreted in the context of a previous study examining the causes of lack of transition, was a first indication that the early formation of small turbulent scales destroyed the coherence of the vortices formed after the first pairing, impeding entrainment and the further formation of small scales.

To ascertain that this physical interpretation is correct, the vorticity and vorticity magnitude budgets were scrutinized at times following each pairing. Consistent with the global growth characteristics, very little vorticity is created on the oxygen side of the layer which contains the heavier fluid. Most of the vorticity is created on the hydrogen side of the layer by the action of the stretching and tilting term. However, even in those regions the negative viscous term dominates the budget of the vorticity magnitude squared, draining vorticity from the system.

Visualizations of the dynamic and thermodynamic variables revealed regions of high density gradient magnitude which mostly exist in the lower LOX stream. These regions are the result of both the distortion of the initial density stratification boundary and the mixing of the two fluids. Due to the very large molar weight ratio between oxygen and hydrogen, parcels of LOX detached from the lower stream will maintain their density identity while being entrained into the upper, lighter hydrogen, thereby creating these large density gradient magnitude regions prior to the complete mixing of the two fluids. Although regions of high density gradient magnitude were

identified also during the mixing of heptane/nitrogen, in that situation there were quantitatively correlated with locations of mixture non-ideality. In contrast, at the conditions of the present simulations the fluid behaves as a perfect gas and an ideal mixture.

Inspection of the irreversible entropy production, which is the dissipation, confirmed that most of the activity is concentrated in the lighter upper stream where most of the small scales are formed. In the lower stream, where most of the high density gradient regions reside, stretching and tilting activity is negligible resulting in the lack of small scales, explaining the inactive dissipation. At all locations, the viscous dissipation dominates both the mass flux and the heat flux dissipation by at least two orders of magnitude.

According to this analysis, two reasons contribute to the lack of mixing transition. First, the relatively large spanwise perturbation induces early small scale formation which destroys the coherence of the vortices formed through pairing, and impedes entrainment and the further formation of small scales. The ultimate vortex resulting from the second pairing is weakened during this process. Second, the regions of high density gradient magnitude formed through the distortion of the initial density stratification boundary and also through mixing of the two species contain very dense fluid in which small turbulent scales cannot form owing to the weakened ultimate vortex.

10 Appendix A

Miscellaneous relationships relevant to the EOS are

$$a_m = \sum_i \sum_j X_i X_j a_{ij}(T)$$

$$b_m = \sum_i X_i b_i$$

where indices here do not follow the Einstein notation, and

$$a_{ij} = 0.457236 \frac{(R_u T_{c,ij})^2}{p_{c,ij}} \alpha_i \alpha_j \quad (54)$$

$$\alpha_i \equiv 1 + C_i - C_i \sqrt{\frac{T}{T_{c,i}}}$$

$$C_i = 0.37464 + 1.54226\Omega_i - 0.26992\Omega_i^2$$

$$b_i = 0.077796 \frac{R_u T_{c,i}}{p_{c,i}}$$

$$T_{c,ij} = (1 - k_{ij}) \sqrt{T_{c,i} T_{c,j}} \text{ with } k_{ii} = 0 \quad (55)$$

$$v_{c,ij} = \frac{1}{8} \left(v_{c,i}^{1/3} + v_{c,j}^{1/3} \right)^3$$

$$Z_{c,ij} = \frac{1}{2} (Z_{c,i} + Z_{c,j})$$

$$p_{c,ij} = \frac{R_u T_{c,ij} Z_{c,ij}}{v_{c,ij}}$$

with $T_{c,i}$, $Z_{c,i}$, $v_{c,i}$ and $p_{c,i}$ being the pure species critical values. Ω_i is the species acentric factor and k_{ij} is an empirical mixing parameter. The values for hydrogen and oxygen are in Table 1, and for comparison the values for heptane and nitrogen are listed as well.

Most data references pertain to k'_{ij} , another mixing parameter related to a_{ij} through

$$k'_{ij} = 1 - \frac{a_{ij}}{\sqrt{a_{ii}a_{jj}}}. \quad (56)$$

Replacing in eq. 56 a_{ij} and $T_{c,ij}$ from eqs. 54 and 55, yields a relationship between the parameters k_{ij} and k'_{ij}

$$(1 - k_{ij}) = (1 - k'_{ij}) \frac{Z_{c,ij}}{v_{c,ij}} \left(\frac{v_{c,i} v_{c,j}}{Z_{c,i} Z_{c,j}} \right)^{1/2}.$$

Given the lack of information regarding the values of k_{ij} or k'_{ij} , in the simulations herein $k_{ij} = 0$.

Acknowledgment

This work was conducted at the Jet Propulsion Laboratory (JPL), California Institute of Technology and sponsored by the National Aeronautics and Space Administration, Marshall Space Flight Center, under the direction of Dr. John Hutt. The computational resources were provided by the JPL Supercomputing Center.

References

- [1] Prausnitz, J., Lichtenthaler, R. and de Azevedo, E., *Molecular Thermodynamics for Fluid-phase Equilibrium*, Prentice-Hall, Inc., 1986
- [2] Hirshfelder, J. O., Curtis, C. F. and Bird, R. B., *Molecular Theory of Gases and Liquids*, John Wiley and Sons, Inc., 1964

- [3] Harstad, K. and Bellan, J., The D^2 Variation for isolated *LOX* drops and poly-disperse clusters in hydrogen at high temperature and pressures, *Combustion and Flame*, 124, 2000
- [4] Mayer, W., Schik, A., Schweitzer, C. and Schaffler, M., Injection and mixing processes in high pressure *LOX*/GH2 rocket combustors AIAA 96-2620, 1996
- [5] Mayer, W., Ivancic, B., Schik, A. and Hornung, U., Propellant atomization in *LOX*/GH2 rocket combustors AIAA 98-3685, 1998
- [6] Chehroudi, B., Talley, D. and Coy, E. Initial growth rate and visual characteristics of a round jet into a sub- to supercritical environment of relevance to rocket, gas turbine and Diesel engines AIAA 99-0206, 1999
- [7] Oschwald, M. and Schik, A., Supercritical nitrogen free jet investigated by spontaneous Raman scattering *Experiments in Fluids*, 27, 497-506, 1999
- [8] Miller, R. S., Harstad, K. and Bellan, J., Direct Numerical Simulations of supercritical fluid mixing layers applied to heptane-nitrogen, *J. Fluid Mech.*, 430, 1-39, 2001
- [9] Okong'o, N. and Bellan, J., Direct Numerical Simulation of a transitional supercritical mixing layer: heptane and nitrogen, submitted for publication to the Journal of Fluid Mechanics, 2000
- [10] Okong'o, N. and Bellan, J., Entropy production of emerging turbulent scales in a temporal supercritical n-heptane/nitrogen three-dimensional mixing layer, *Proc. Comb. Inst.*, Vol. 28, 497-504, 2000
- [11] Harstad, K. and Bellan, J., The Lewis number under supercritical conditions, *Int. J. Heat and Mass Transfer*, 42, 961-970, 1999
- [12] Okong'o, N., Bellan, J. and Harstad, K., Consistent boundary conditions for multicomponent real gas mixtures based on characteristic waves, submitted for publication to the Journal of Computational Physics, 2000
- [13] Sarman, S. and Evans, D. J., Heat flux and mass diffusion in binary Lennard-Jones mixtures, *Phys. Rev.*, A45(4), 2370-2379, 1992
- [14] Harstad, K. and J. Bellan, J., An all-pressure fluid-drop model applied to a binary mixture: heptane in nitrogen, *Int. J. Multiphase Flow*, 26(10), 1675-1706, 2000
- [15] Harstad, K. Miller, R. S. and J. Bellan, J., Efficient high-pressure state equations, *A.I.Ch.E. J.*, 43(6), 1605-1610, 1997

- [16] Harstad, K, and J. Bellan, J., Isolated Liquid Oxygen Drop Behavior in Fluid Hydrogen at Rocket Chamber Pressures, *Int. J Heat and Mass Transfer*, 41, 3537-3550, 1998
- [17] Kennedy, C. A. and Carpenter, M. H., Several new numerical methods for compressible shear-layer simulations *App. Num. Math.* 14, 397-433, 1994
- [18] Muller, S. M. and Scheerer, D., A method to parallelize tridiagonal solvers, *Parallel Computing*, 17, 181-188, 1991
- [19] Drazin, P. G. and Reid, W. H., *Hydrodynamic Stability* Cambridge University Press, 1981
- [20] Moser, R. D. and Rogers, M. M., Mixing transition and the cascade to small scales in a plane mixing layer, *Phys. Fluids A* 3(5), 1128-1134, 1991
- [21] Okong'o, N. and Bellan, J., Linear stability analysis of supercritical two- and three-dimensional mixing layers, submitted for publication to *Physics of Fluids*, 2001
- [22] Moser, R. D. and Rogers, M. M., The three-dimensional evolution of a plane mixing layer: pairing and transition to turbulence, *J. Fluid Mech.*, 247, 275-320, 1993
- [23] Cortesi, A. B., Smith, B. L., Yadigaroglu, G. and Banerjee, S., Numerical investigation of the entrainment and mixing processes in neutral and stably-stratified mixing layers, *Phys. Fluids* 11(1), 162-185, 1999
- [24] Miller, R. S. and J. Bellan, J., Direct Numerical Simulation and Subgrid Analysis of a Transitional Droplet Laden Mixing Layer, *Phys. Fluids*, 12(3), 650-671, 2000
- [25] Rogers, M. M. and Moser, R. D., Spanwise scale selection in plane mixing layers, *J. Fluid Mech.*, 247, 321-337, 1993
- [26] Hannoun, I., Fernando, H. and List, E. 1988 Turbulence structure near a sharp density interface *J. Fluid Mech.* 189, 189-209, 1988
- [27] Cortesi, A. B., Yadigaroglu, G. and Banerjee, S., Numerical investigation of the formation of three-dimensional structures in stably-stratified mixing layers, *Phys. Fluids* 10(6), 1449-1473, 1998

Species	m (g/mol)	T_c (K)	p_c (MPa)	v_c (cm ³ /mol)	Z_c	Ω
Hydrogen	2.0159	33.0	1.2838	64.284	0.306	-0.216
Nitrogen	28.013	126.26	3.399	89.8	0.290	0.039
Oxygen	31.9988	154.58	5.0430	73.368	0.288	0.025
Heptane	100.205	540.2	2.74	432.0	0.263	0.35

Table 1: Pure species properties.

Mean quantity	$x_2 = -\infty$ (Oxygen)	$x_2 = \infty$ (Oxygen)
\bar{u}_1 (m/s)	-193.732	193.732
a_s (m/s)	484.329	484.329
$\bar{\rho}$ (kg/m ³)	63.191	63.191
p (atm)	100	100
T (K)	600	600
Y_O	1	1

Table 2: Mean flow properties $\rho_2/\rho_1=1$.

Mean quantity	$x_2 = -\infty$ (Oxygen)	$x_2 = \infty$ (Hydrogen)
\bar{u}_1 (m/s)	-187.287	666.798
a_s (m/s)	467.045	1671.193
$\bar{\rho}$ (kg/m ³)	68.271	5.298
p (atm)	100	100
T (K)	556	444
Y_O	1	0

Table 3: Mean flow properties $\rho_2/\rho_1=12.88$.

Mean quantity	$x_2 = -\infty$ (Oxygen)	$x_2 = \infty$ (Hydrogen)
\bar{u}_1 (m/s)	-158.004	770.983
a_s (m/s)	397.517	1915.376
$\bar{\rho}$ (kg/m ³)	96.764	3.965
p (atm)	100	100
T (K)	400	600
Y_O	1	0

Table 4: Mean flow properties $\rho_2/\rho_1=24.40$.

Case	Flow type	$\frac{\rho_2}{\rho_1}$	$\alpha\delta_\omega$	$\alpha\delta_\omega \frac{c_i}{\bar{U}}$	$\frac{c_{re}}{\bar{U}}$	$\frac{\lambda_1}{\delta_\omega} = \frac{2\pi}{\alpha\delta_\omega}$
1	Variable density ¹ ($a_s = 10^6$)	1.00	0.860	0.3830	0.6598	7.31
2	Variable density ²	1.00	0.797	0.3151	0	7.88
3	Variable density ²	12.88	0.670	0.1756	-0.0747	9.38
4	Variable density ²	24.40	0.607	0.1284	-0.0745	10.35

¹Same velocity profile as for Case 4.

²Velocity profile from Equation 32, $M_{c,0} = 0.4$.

Table 5: Most unstable wavelength, two-dimensional analysis.

Run	Re_0	$L_1 \times L_2 \times L_3$	$N_1 \times N_2 \times N_3$	$\max Re_m$	t_{\max}^*	Timesteps	CPU(h)
R600	600	$0.2 \times 0.232 \times 0.12$	$288 \times 336 \times 176$	1014	127.45	3730	5472
R750	750	$0.2 \times 0.2 \times 0.12$	$352 \times 352 \times 208$	1680	190.44	6860	13214

Table 6: Listing of the simulations and associated resolution. L_i is in meters.

$ \nabla\rho _{\text{cutoff}}$	Braid plane:	Between-the-braid plane:
$K \nabla\rho _{\max}$	$ \nabla\rho _{\max} = 2.440 \times 10^4 \text{ kg/m}^4$	$ \nabla\rho _{\max} = 1.955 \times 10^4 \text{ kg/m}^4$
$K = 0.4$	0.954	0.956
$K = 0.3$	0.945	0.951
$K = 0.2$	0.930	0.949
$K = 0.1$	0.906	0.923

Table 7: Conditional averages over regions where $|\nabla\rho| > \text{cutoff}$. The calculations are made at $t^* = 150$ for R750.

	Braid plane	Between-the-braid plane	Global
$Y_O, \nabla\rho $ Correlation	0.34	0.37	0.35

Table 8: Correlations with $|\nabla\rho|$ at $t^* = 150$ for R750.

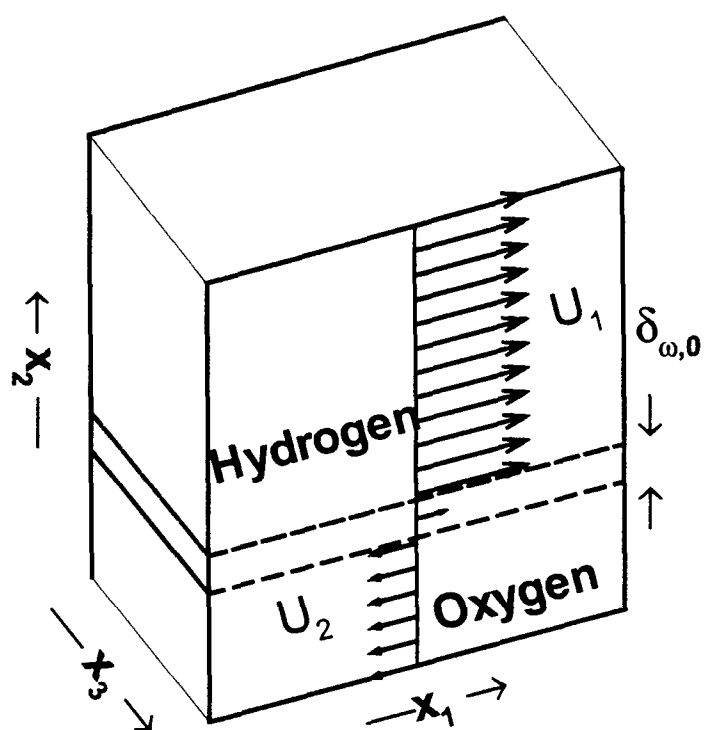


Figure 1: Sketch of the mixing layer configuration.

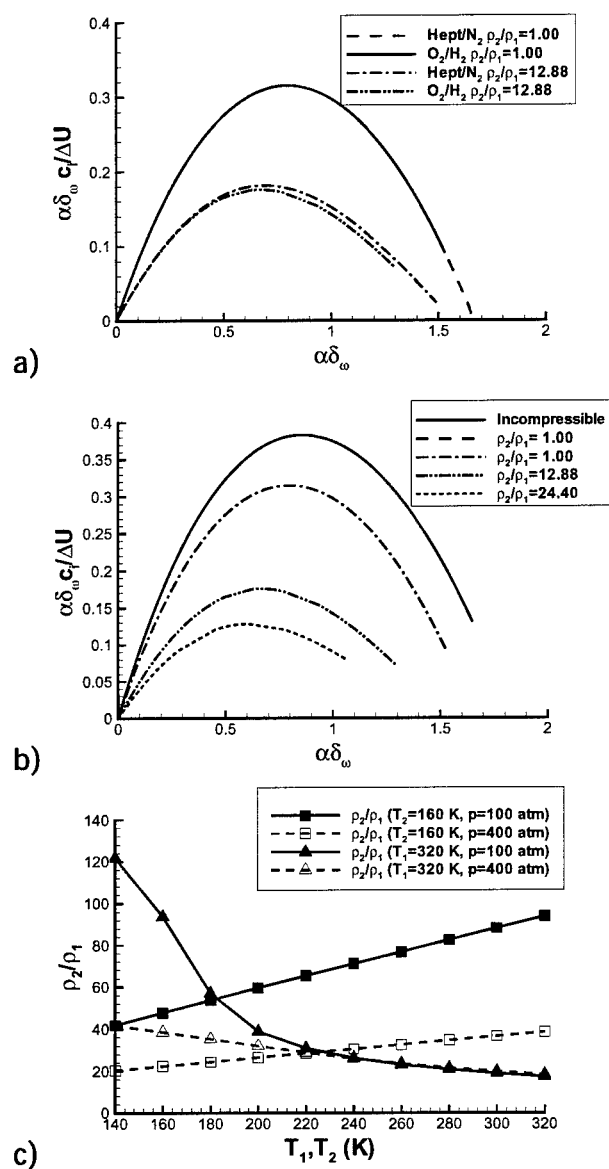


Figure 2: a) Comparison of the stability curves for heptane/nitrogen (at 60 atm) and oxygen/hydrogen (at 100 atm), b) stability curves for oxygen/hydrogen (at 100 atm) and c) density ratio versus temperature for oxygen/hydrogen.

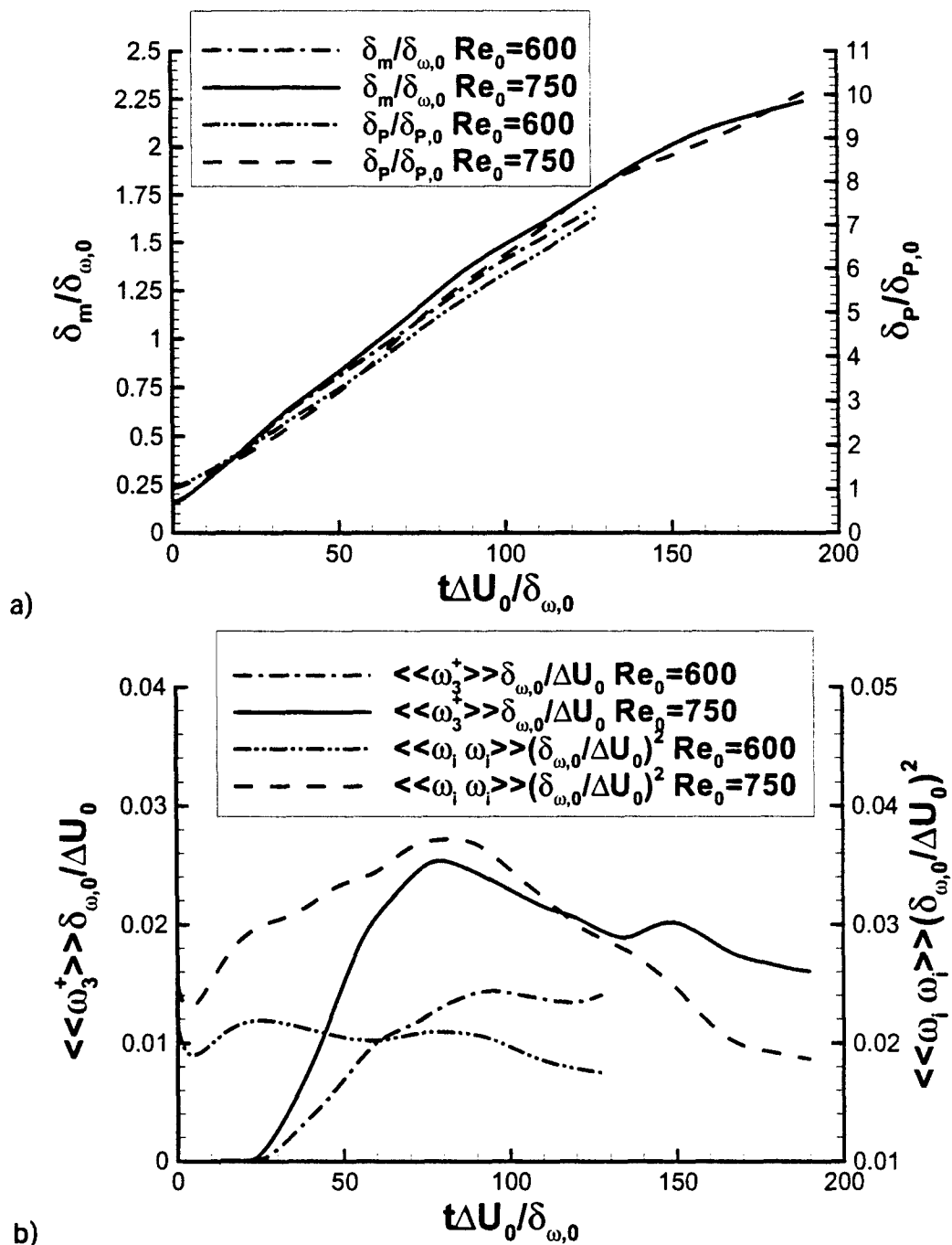


Figure 3: Time evolution of a) momentum and product thicknesses and b) global spanwise vorticity and enstrophy.

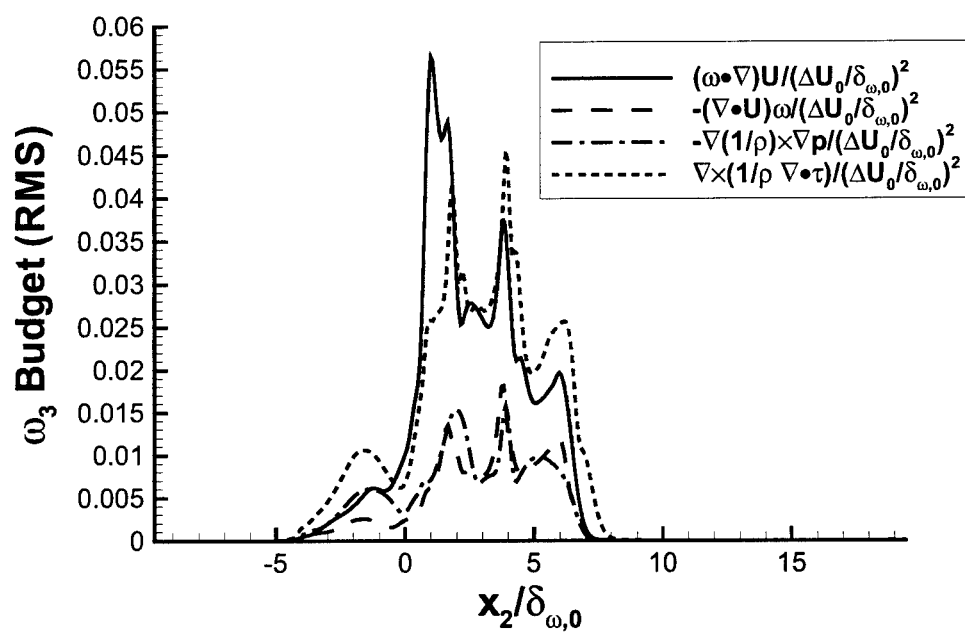
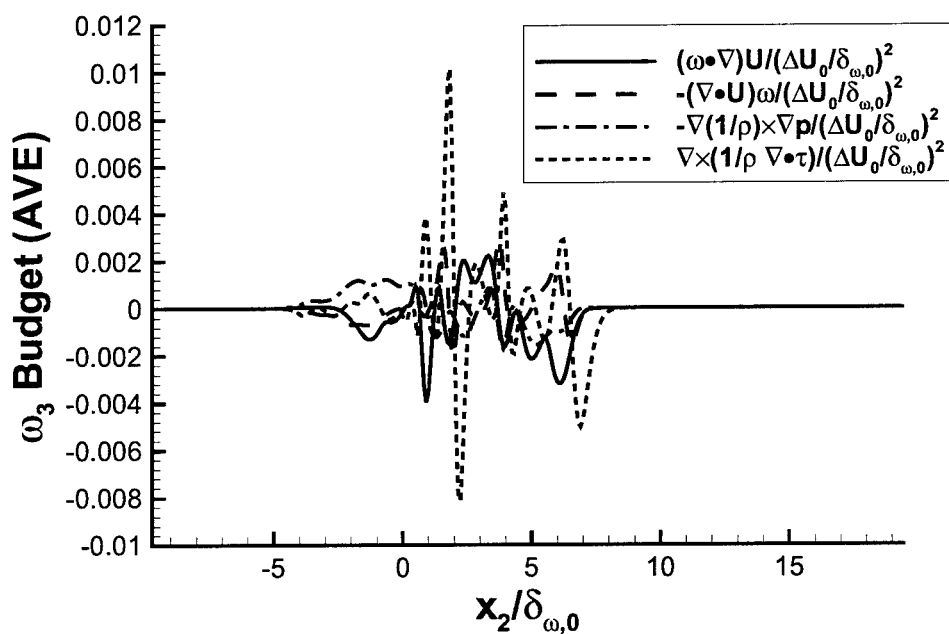


Figure 4: Vorticity budget for R750 at $t^*=80$: Spanwise vorticity, a) plane average and b) plane RMS, and vorticity magnitude, c) plane average and d) plane RMS.

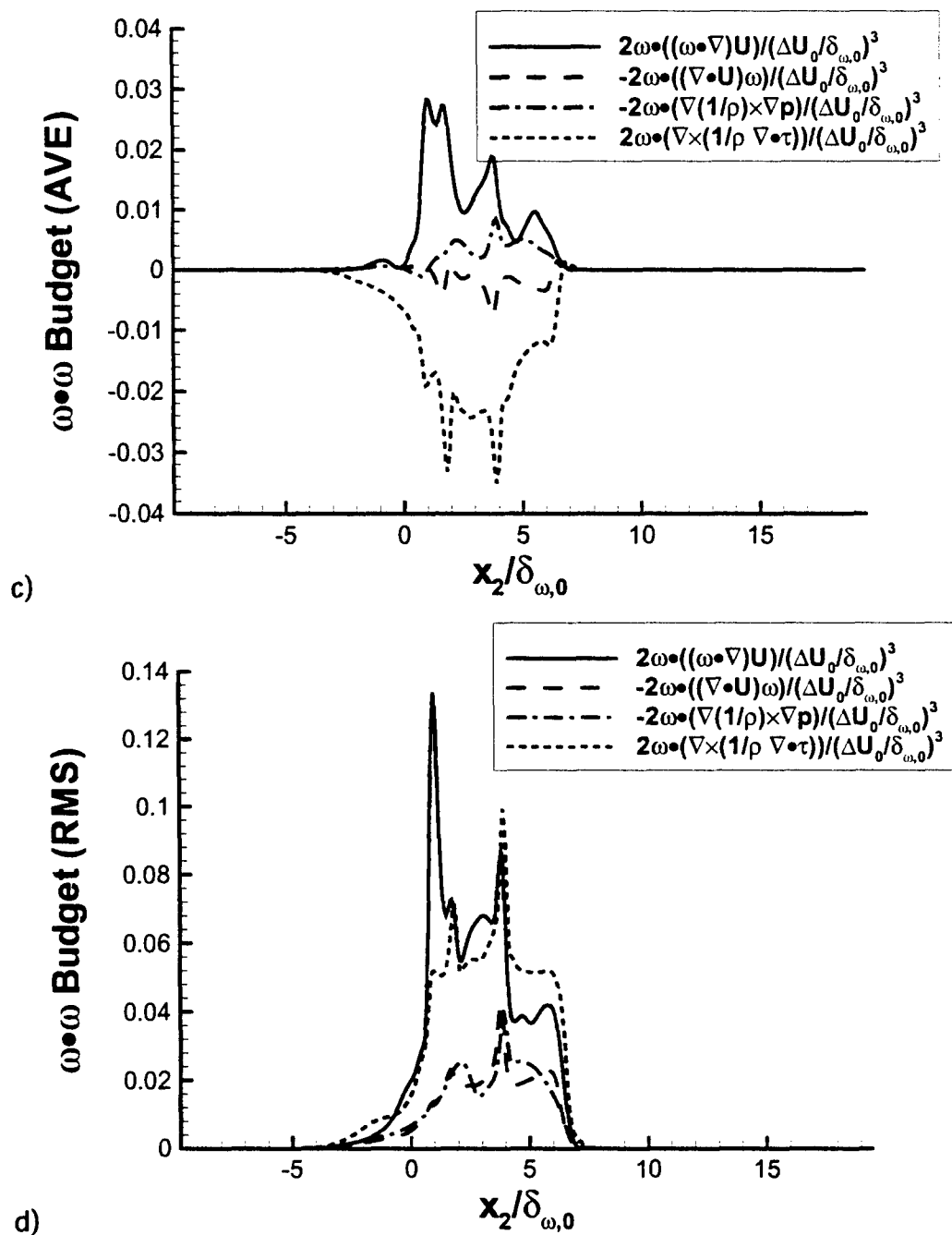


Figure 4: (continued) Vorticity budget for R750 at $t^* = 80$: Spanwise vorticity, a) plane average and b) plane RMS, and vorticity magnitude, c) plane average and d) plane RMS.

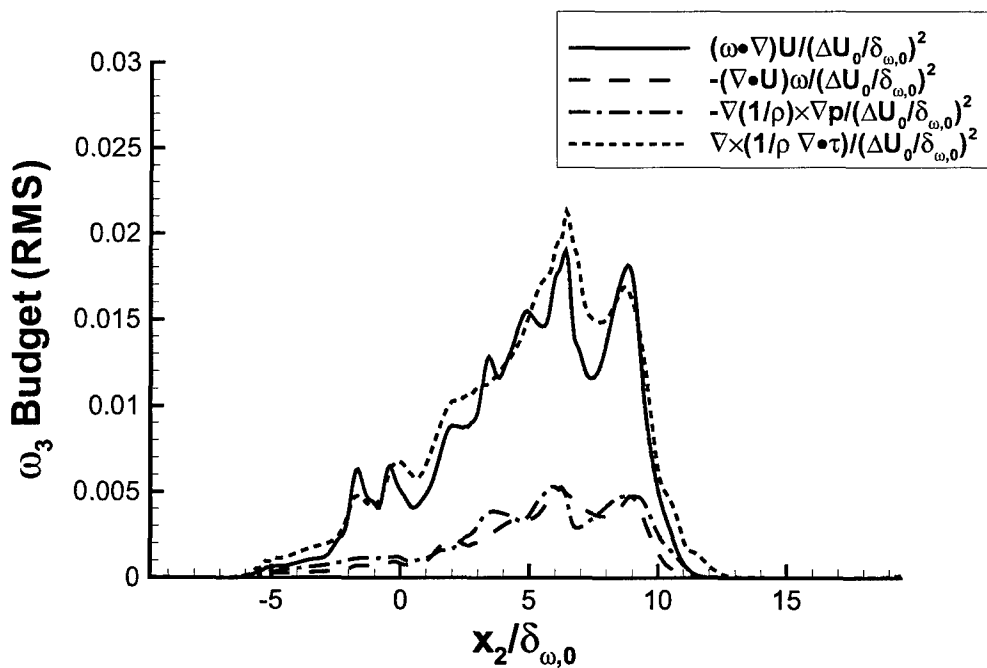
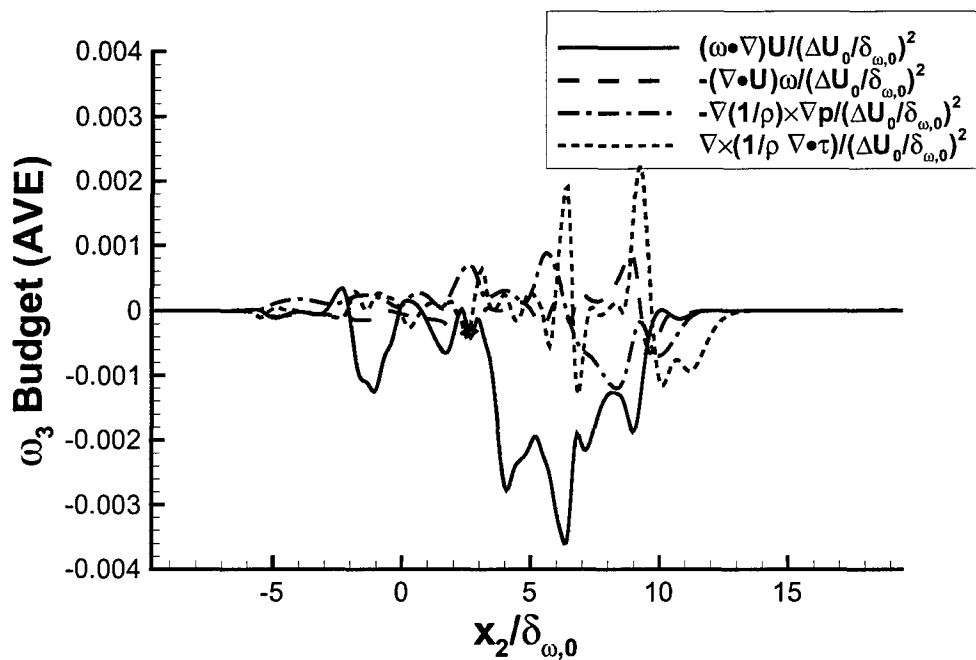


Figure 5: Vorticity budget for R750 at $t^* = 150$: spanwise vorticity, a) plane average and b) plane RMS, and vorticity magnitude, c) plane average and d) plane RMS.

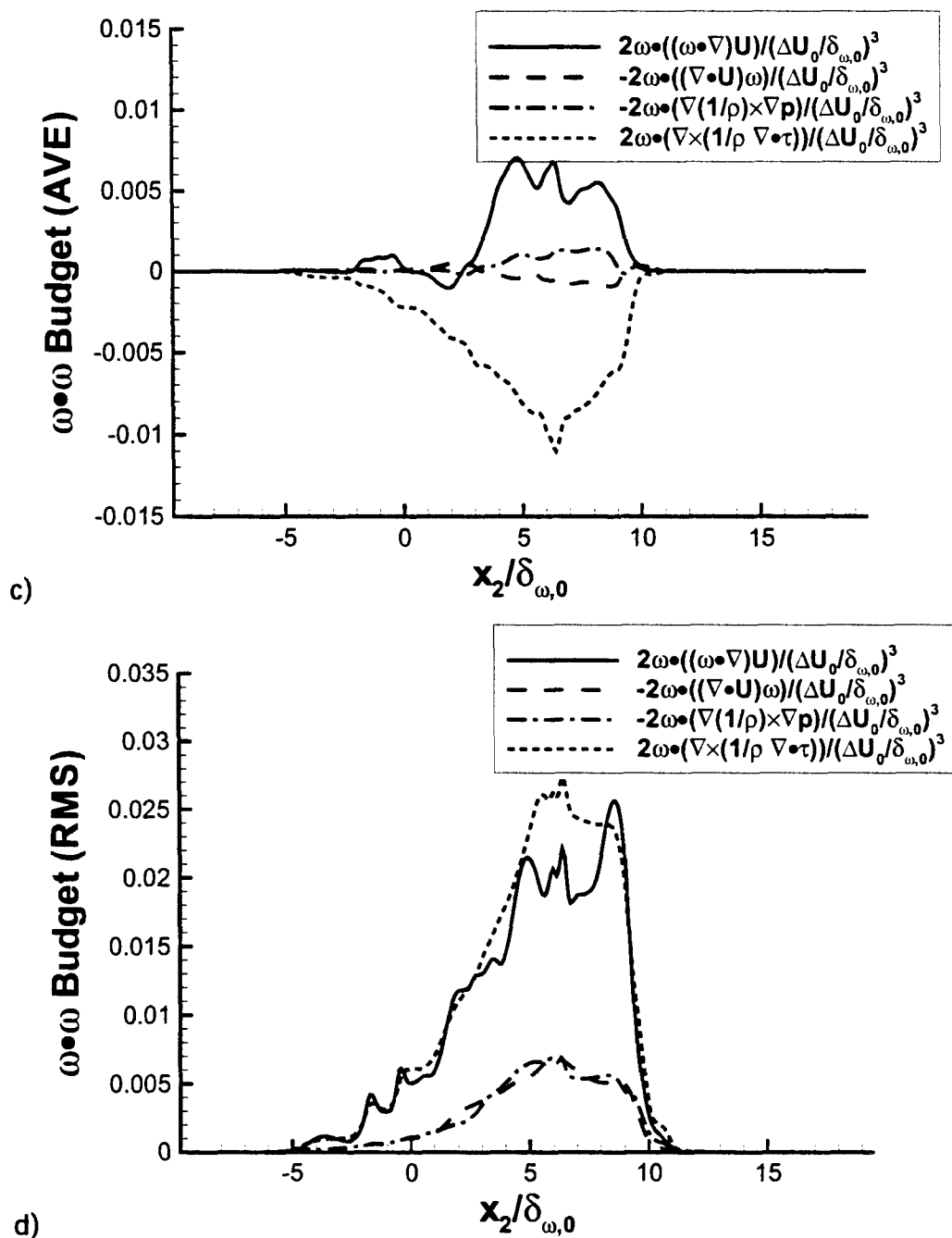


Figure 5: (continued) Vorticity budget for R750 at $t^*=150$: spanwise vorticity, a) plane average and b) plane RMS, and vorticity magnitude, c) plane average and d) plane RMS.

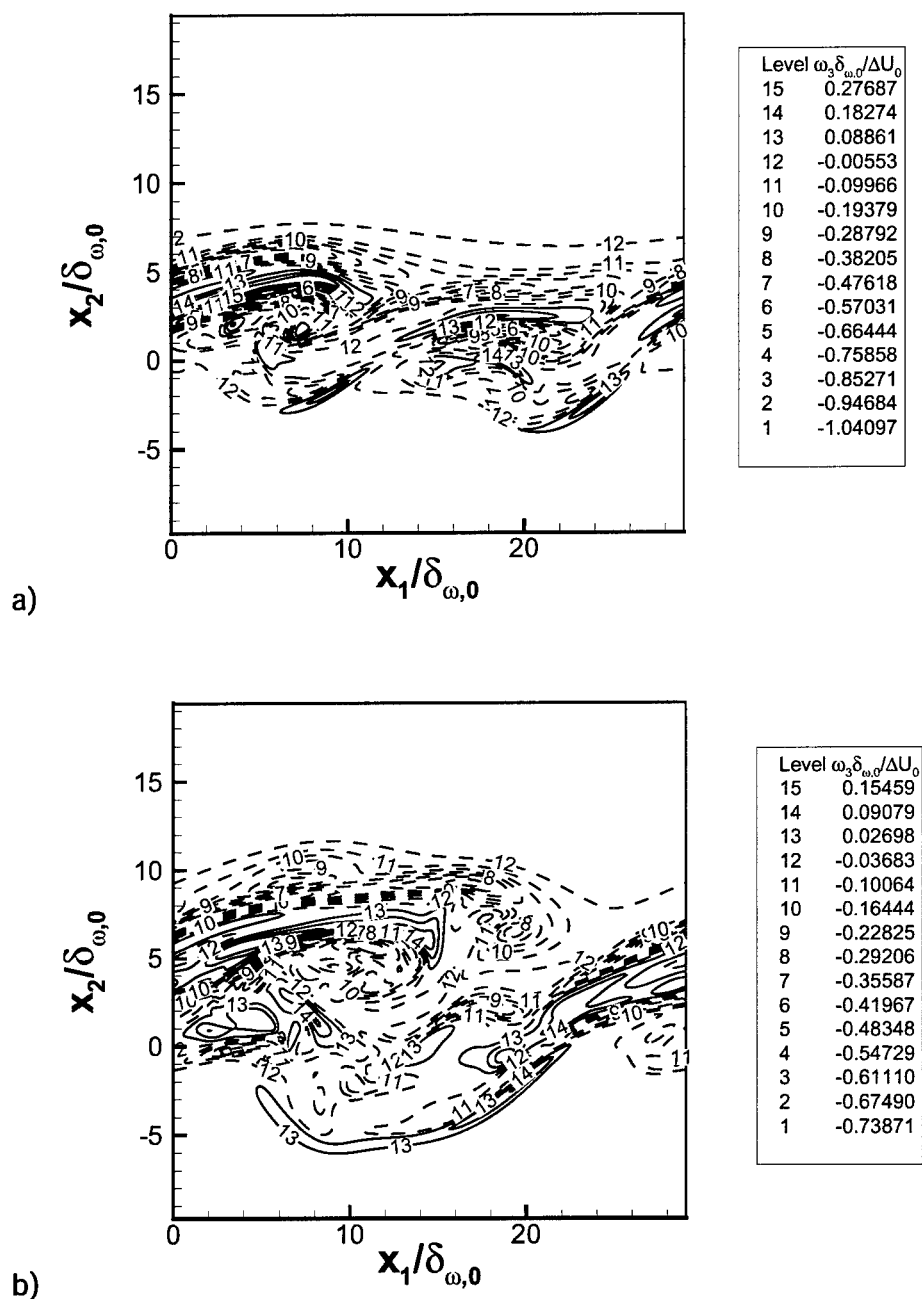


Figure 6: Nondimensional spanwise vorticity for R750 in the braid plane ($x_3 = L_3/16$) at a) $t^*=80$ and b) $t^*=150$.

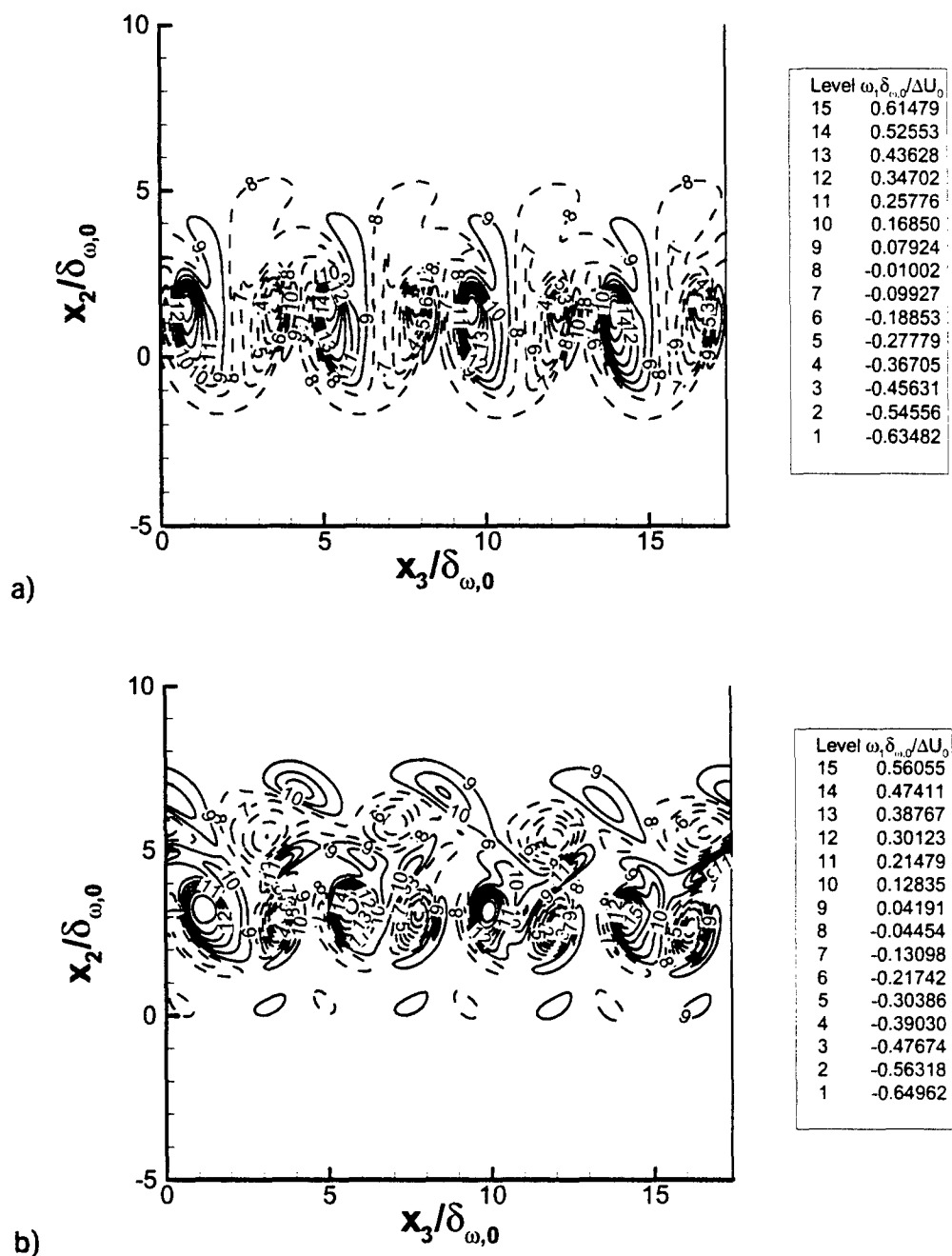


Figure 7: Nondimensional streamwise vorticity for R750 in the streamwise mid-braid plane ($x_1/\delta_{\omega,0}=25.6$) at a) $t^*=80$ and b) $t^*=150$.

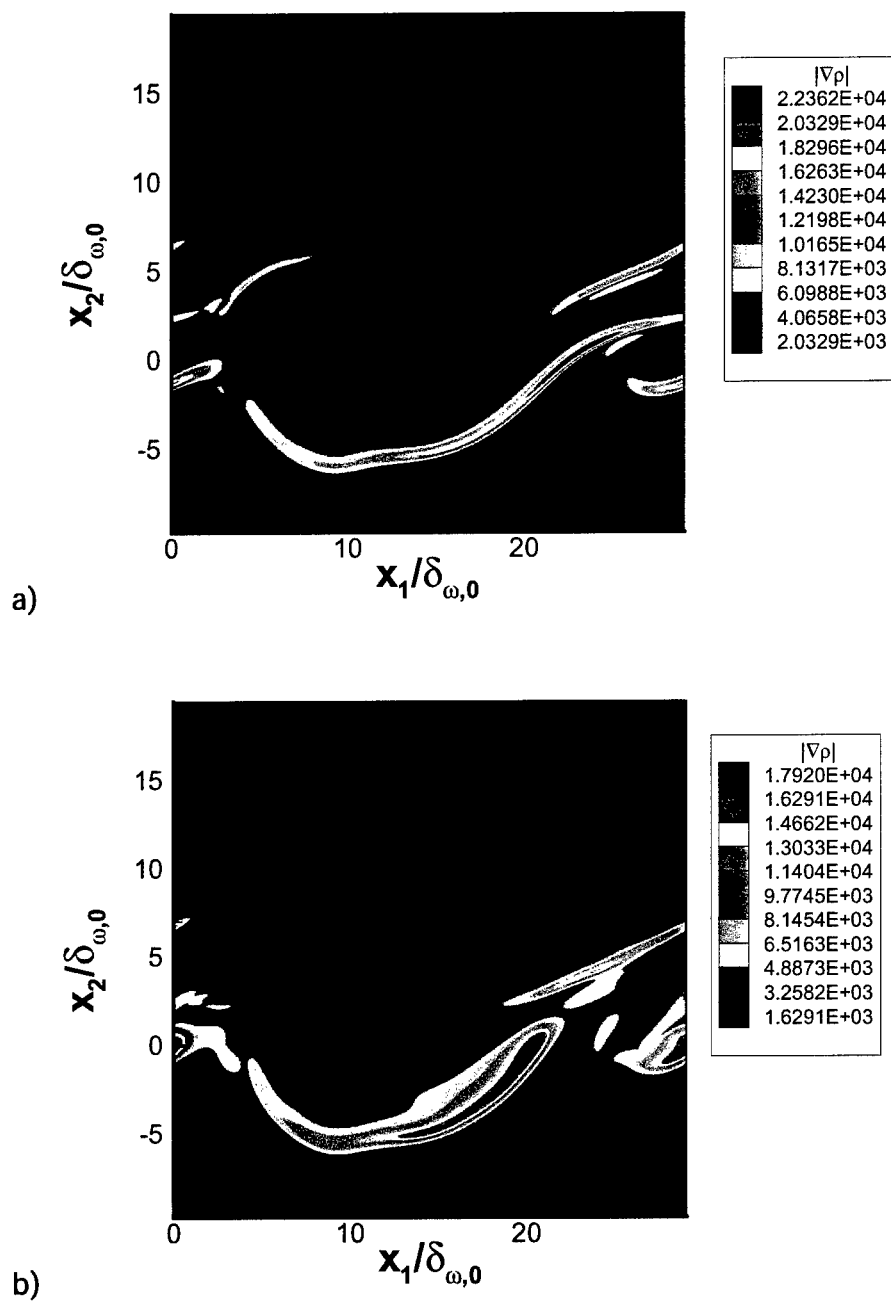


Figure 8: Density gradient magnitude (in kg/m⁴) for R750 at $t^*=150$, a) in the braid plane ($x_3 = L_3/16$) and b) in the between-the-braid plane ($x_3 = L_3/2$).

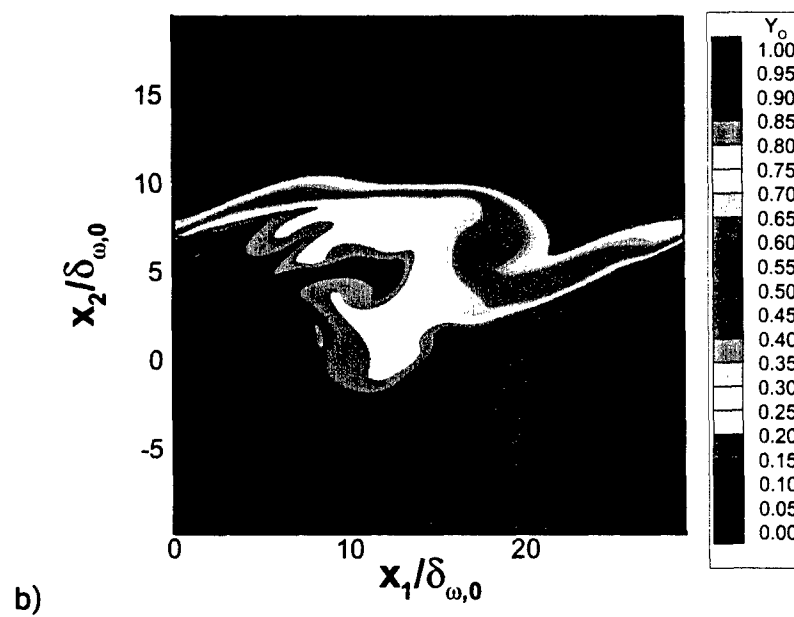
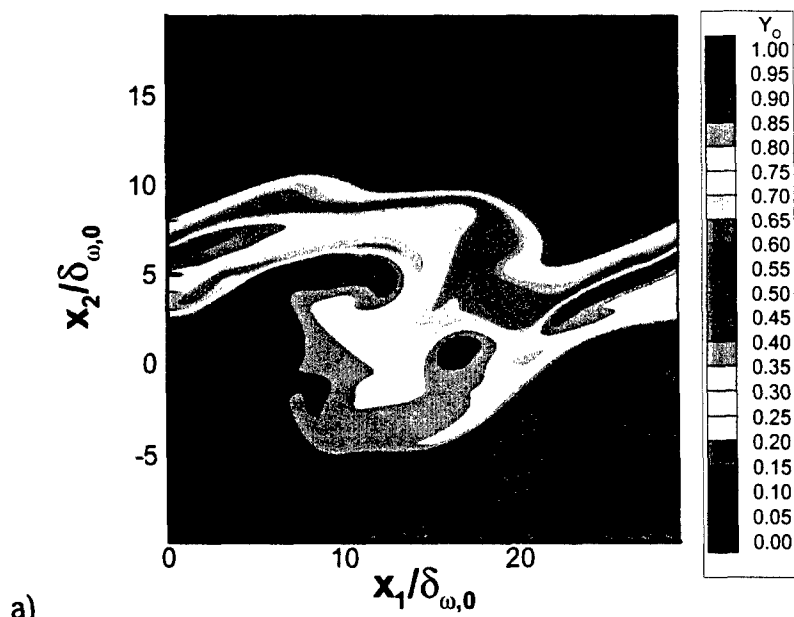


Figure 9: Oxygen mass fraction for R750 at $t^*=150$, a) in the braid plane, b) in the between-the-braid plane and c) in the streamwise mid-braid plane.

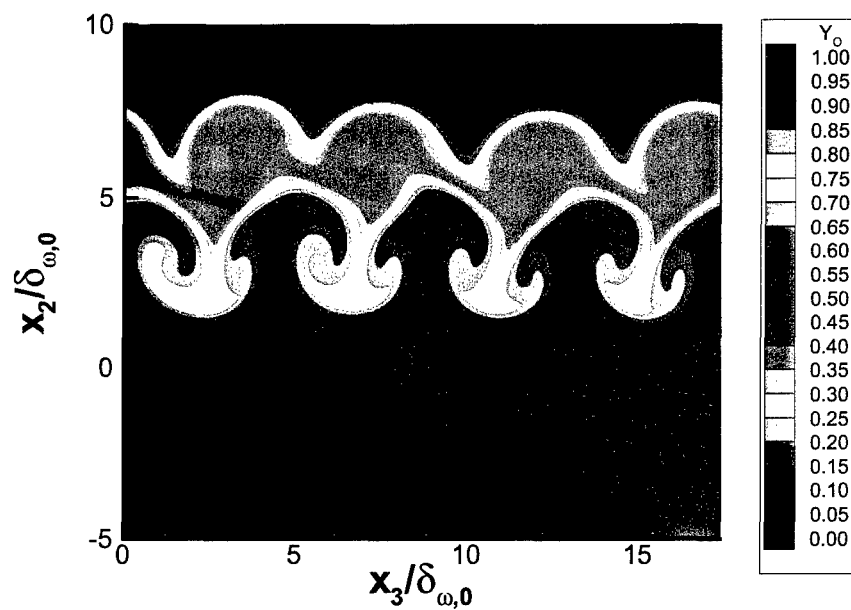


Figure 9: (continued) Oxygen mass fraction for R750 at $t^*=150$, a) in the braid plane, b) in the between-the-braid plane and c) in the streamwise mid-braid plane.

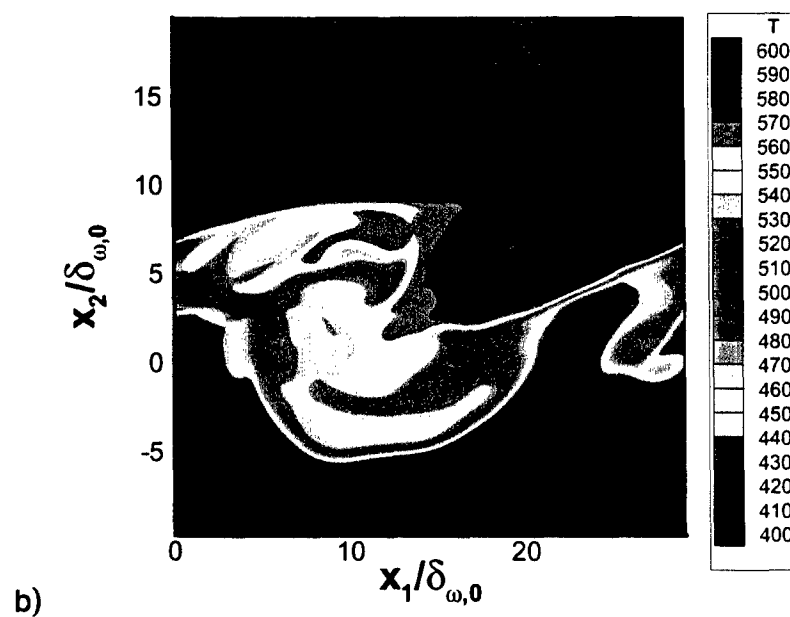
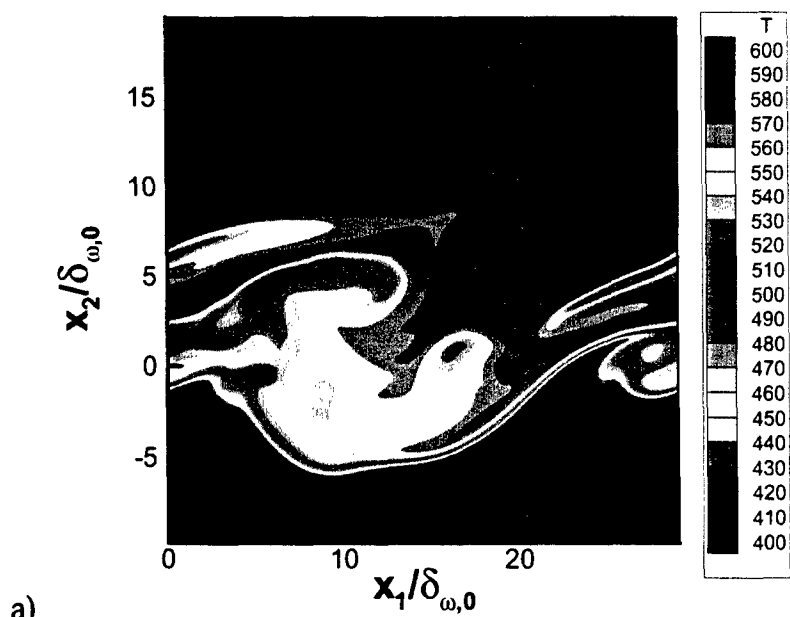


Figure 10: Temperature (in Kelvin) for R750 at $t^*=150$, a) in the braid plane and b) in the between-the-braid plane.

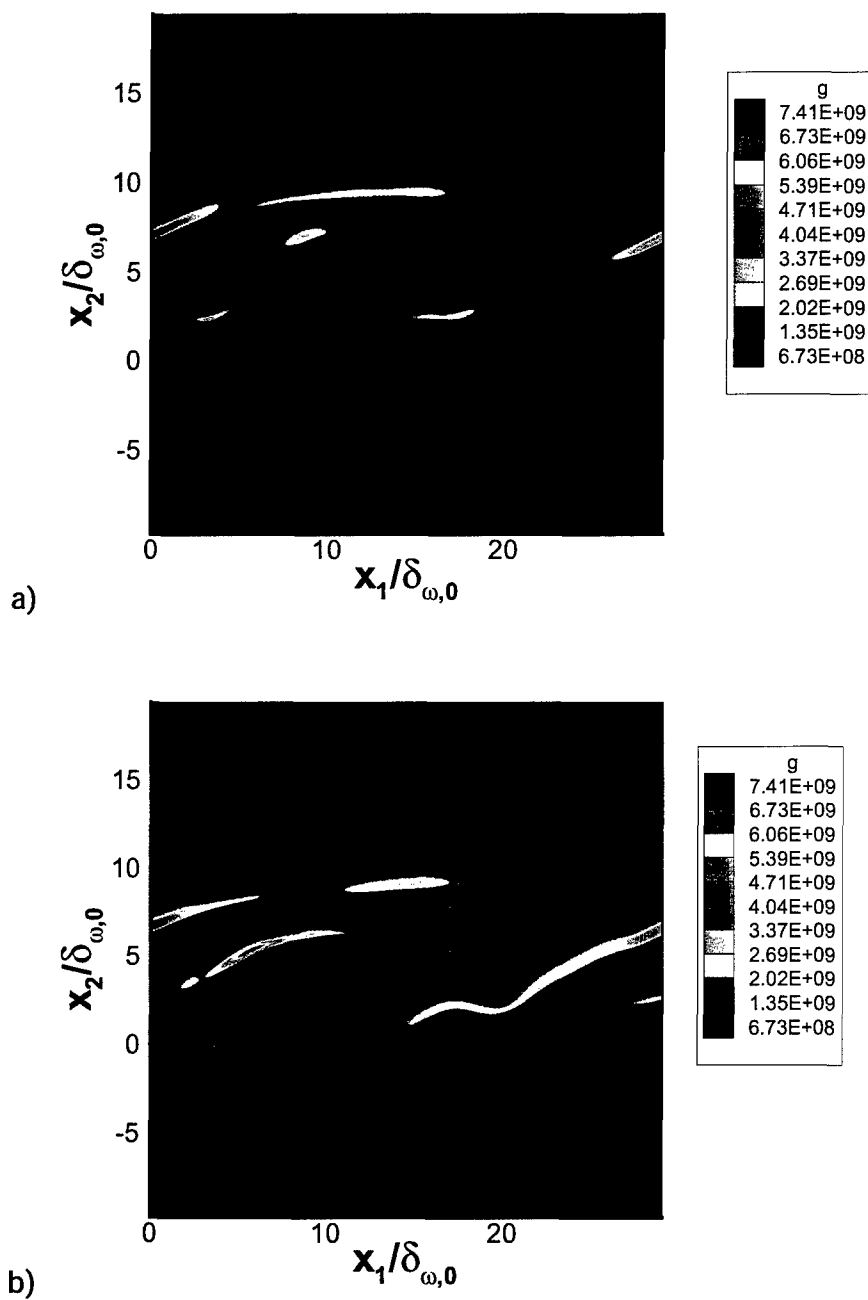


Figure 11: Dissipation (in J/m³K) for R750 at $t^* = 150$, a) in the braid plane and b) in the between-the-braid plane.

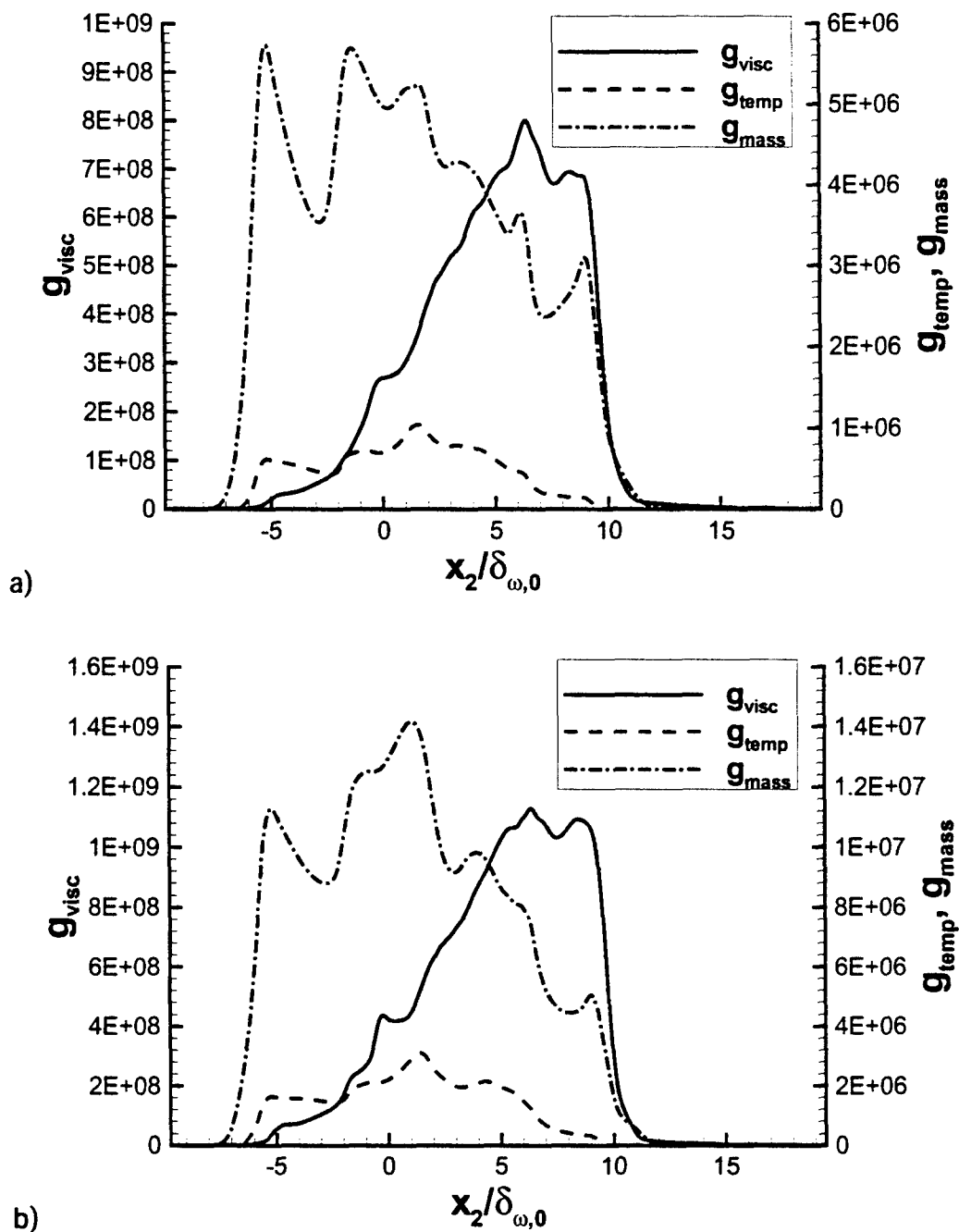


Figure 12: Contributions to the dissipation (in $\text{J/m}^3\text{K}$) for R750 at $t^* = 150$, a) plane average and b) plane RMS.